

1 **Solar radiation estimation in West Africa: impact of dust conditions during**
2 **2021 dry season**

3

4 Léo Clauzel¹, Sandrine Anquetin¹, Christophe Lavaysse¹, Gilles Bergametti², Christel
5 Bouet^{2,3}, Guillaume Siour⁴, Rémy Lapere¹, Béatrice Marticorena⁴, Jennie Thomas¹

6

7 ¹Université Grenoble Alpes, IRD, CNRS, Grenoble-INP, IGE, 38000 Grenoble, France

8 ²LISA, Université Paris Cité and Univ Paris Est Créteil, CNRS, F-75013 Paris, France

9 ³Institut d'Ecologie et des Sciences de l'Environnement de Paris, UMR IRD 242, Univ Paris
10 Est Créteil–Sorbonne Université–CNRS–INRAE–Université Paris Cité, F-93143 Bondy,
11 France

12 ⁴LISA, Univ Paris Est Créteil, Université Paris Cité, CNRS, LISA, F-94010 Créteil, France

13

14 *Correspondence to:* Léo Clauzel (leo.clauzel@univ-grenoble-alpes.fr)

15 **Abstract**

16 The anticipated increase in solar energy production in West Africa requires high-quality solar
17 irradiance estimates, which is affected by meteorological conditions and in particular the
18 presence of desert dust aerosols. This study examines the impact of incorporating desert
19 dust into solar irradiance and surface temperature estimations. The research focuses on a
20 case study of a dust event in March 2021, which is characteristic of the dry season in West
21 Africa. Significant desert aerosol emissions at the Bodele depression are associated with a
22 Harmattan flow that transports the plume westwards. Simulations of this dust event were
23 conducted using the WRF meteorological model alone, as well as coupled with the
24 CHIMERE chemistry-transport model, using three different datasets for the dust aerosol
25 initial and boundary conditions (CAM5, GOCART, MERRA2). Results show that considering
26 desert dust reduces estimation errors in global horizontal irradiance (GHI) by about 75%.
27 The dust plume caused an average 18% reduction in surface solar irradiance during the
28 event. Additionally, the simulations indicated a positive bias in aerosol optical depth (AOD)
29 and PM10 surface concentrations. The choice of dataset for initial and boundary conditions
30 minimally influenced GHI, surface temperature, and AOD estimates, whereas PM10
31 concentrations and aerosol size distribution were significantly affected. This study
32 underscores the importance of incorporating dust aerosols into solar forecasting for better
33 accuracy.

34

35 **Short summary**

36 Solar energy production in West Africa is set to rise, needing accurate solar irradiance
37 estimates, which is affected by desert dust. This work analyses a March 2021 dust event
38 using a modelling strategy incorporating desert dust. Results show that considering desert
39 dust cut errors in solar irradiance estimates by 75% and reduces surface solar radiation by
40 18%. This highlights the importance of incorporating dust aerosols into solar forecasting for
41 better accuracy.

42

43 **1. Introduction**

44 The West African region is facing significant development challenges due to global change.
45 One of these challenges is related to access to electricity, particularly through the use of
46 renewable energy. West African countries have committed to reduce their greenhouse gas
47 emissions as part of the Paris Agreement (2015). Furthermore, assessments of solar
48 resources in West Africa demonstrate the region's substantial potential, as shown by
49 Diabaté et al. (2004), Plain et al. (2019) and Yushchenko et al. (2018). The International
50 Energy Agency (IEA) projects that the installed capacity for photovoltaic (PV) power
51 generation will increase by almost 20 times from 2020 to 2030 under its Sustainable Africa
52 Scenario (IEA, 2022). PV energy is expected to experience significant growth due to its
53 competitiveness and low-carbon nature. However, solar production is highly dependent on
54 weather conditions (Dajuma et al., 2016).

55 The growth of solar energy in West Africa calls for the development of tailored tools to
56 facilitate its integration into power grids and ensure optimal operational maintenance.
57 Accurate production forecasts are required by solar power plant operators, spanning various
58 timescales, ranging from a few hours to several days. This is essential for maximising
59 production, reducing penalties linked to predicted deliverable energy, and optimising plant
60 maintenance to minimise production losses. High-quality forecasts are also crucial for
61 electricity grid operators to maintain supply-demand equilibrium and ensure system stability.
62 Therefore, the variability of energy production significantly affects them. The key

63 meteorological variables that influence photovoltaic production are the Global Horizontal
64 Irradiance (GHI) and the air temperature. These factors, which directly impact electricity
65 production and cell efficiency, often reach high levels in this region as demonstrated by
66 Dajuma et al. (2016) and Ziane et al. (2021). Their findings indicate that solar irradiance is
67 the primary factor influencing PV production, as the generated current by the photoelectric
68 effect is proportional to the irradiance. Furthermore, they demonstrate that, at the second
69 order, the air temperature affects the efficiency of solar cells, as both parameters are
70 inversely correlated.

71
72 Clauzel et al. (2024) identified desert dust aerosol as a significant source of GHI forecast
73 errors for the only two solar power plants in the Sahel region of Sococim (Senegal) and
74 Zagtoui (Burkina Faso), particularly during the dry season. Dust aerosols are a key element
75 in the West African climate and strongly influence solar farm production through their direct
76 effect (aerosol-radiation interaction (ARI), Briant et al., 2017) and indirect effects (aerosol-
77 cloud interaction (ACI), Tuccella et al., 2019) on radiation, and also through their deposition
78 on solar panels (fouling effect, Diop et al., 2020, Aidara et al., 2023). As mentioned by Kok et
79 al. (2021), the West African desert aerosol load is the highest in the world and occurs mainly
80 during the dry season. In fact, North Africa, including the Sahara, is the world's largest
81 contributor to desert dust emissions (Prospero et al., 2002), and 60% of this dust is
82 transported to the West African region (D'Almeida, 1986; Kok et al., 2021). Most dust
83 emissions are associated with synoptic-scale atmospheric dynamics such as the Harmattan
84 flow during the dry season (Klose et al., 2010). Engelstaedter and Washington (2007)
85 pointed out the importance of small-scale wind events associated with the large-scale flow,
86 especially in the Bodele depression, which is a hotspot for dust emissions (Engelstaedter et
87 al., 2006). Analysing satellite observations, Schepanski et al. (2009) show that 65% of the
88 activation of the dust source area occurred in the early morning, demonstrating the important
89 role of the breakdown of the nocturnal low-level jet. Washington and Todd (2005) confirmed
90 the importance of the Bodele low-level jets during the dry season in initiating dust emissions
91 that can be transported to the West African coast within a few days. Dust aerosol emissions
92 are also highly linked to Mesoscale Convective Systems (MCS, Marsham et al., 2008 ;
93 Bergametti et al., 2017) and to strong near-surface winds in the intertropical discontinuity
94 zone during the rainy season (Bou Karam et al., 2009).

95
96 Some studies intend to model dust events in West Africa such as Ochiegbu (2021) who
97 implemented a back-trajectories model to understand the dust event reaching Nigeria. This
98 work revealed that most of the aerosols coming to Nigeria between 2011 and 2014 were
99 originating from the Bodele Depression. Menut (2023) focused on dust forecasting during the
100 Cloud-Atmospheric Dynamics-Dust Interactions in West Africa (CADDIWA) campaign during
101 summer 2021 (Flamant et al., 2024) using the CHIMERE regional chemistry-transport model
102 (Menut et al., 2021). The model was coupled online with the Weather Research and
103 Forecasting (WRF) meteorological model (Briant et al., 2017; Tuccella et al., 2019) to
104 perform dust aerosol concentration forecasts. The results of this work provide confidence in
105 the model coupling in the region as the dust forecast quality does not decrease with time
106 over a few days. In addition, only a limited number of studies have been conducted on the
107 prediction of GHI in the West African region. Sawadogo et al. (2024) conducted an
108 evaluation of WRF-solar GHI forecast (Jimenez et al., 2016) in Ghana for the year 2021. In
109 their work, a version of the model coupled offline with Copernicus Atmosphere Monitoring
110 Service (CAMS) Aerosol Optical Depth (AOD) forecasts was considered to integrate

111 information on aerosol load. They showed that WRF-Solar outperforms in predicting GHI
112 under clear sky conditions while its performance under high aerosol levels remains poor, that
113 was mainly attributed to uncertainties in the input AOD during data assimilation within the
114 model. Close to the region of interest, for the northern Morocco area, El Alani et al. (2020)
115 compared the performance of global models (Global Forecast System, Integrated Forecast
116 System, McClear) and demonstrated their proficiency in capturing GHI hourly temporal
117 variability.

118

119 As far as our knowledge is concerned, no studies have been conducted to assess online
120 coupled simulations between a meteorological model and an aerosol life cycle model
121 representing the emissions, the transport and the deposition in West Africa to estimate solar
122 irradiance. This is despite the significant presence of desert dust, characterised by high
123 concentrations in the region. Additionally, scarce attention has been given to the significance
124 of initial and boundary conditions for conducting the aerosol model on the performance of
125 analysis simulations, and to our knowledge, investigating these aspects would represent a
126 novel contribution to research in the West African region.

127

128 Within this general context, the objectives of this study are two folds i) to evaluate the ability
129 to reproduce a dust event using a meteorological and dust life cycle model coupling
130 configuration, and ii) to investigate whether the performance of the simulations can be
131 enhanced by modifying the aerosol initial and boundary conditions employed, and to
132 estimate the uncertainty associated with this dataset selection with regard to the errors made
133 by the model. Section 2 introduces the case study, the simulation configuration, the data and
134 models selected for this work. In Section 3, the results are presented, beginning with the
135 variables of interest for solar production (GHI and surface air temperature), followed by the
136 variables associated with the desert aerosols (AOD, concentration, size distribution,
137 emissions). Section 4 gives main conclusions and draws some perspectives for this study.

138

139 **2. Material and methods**

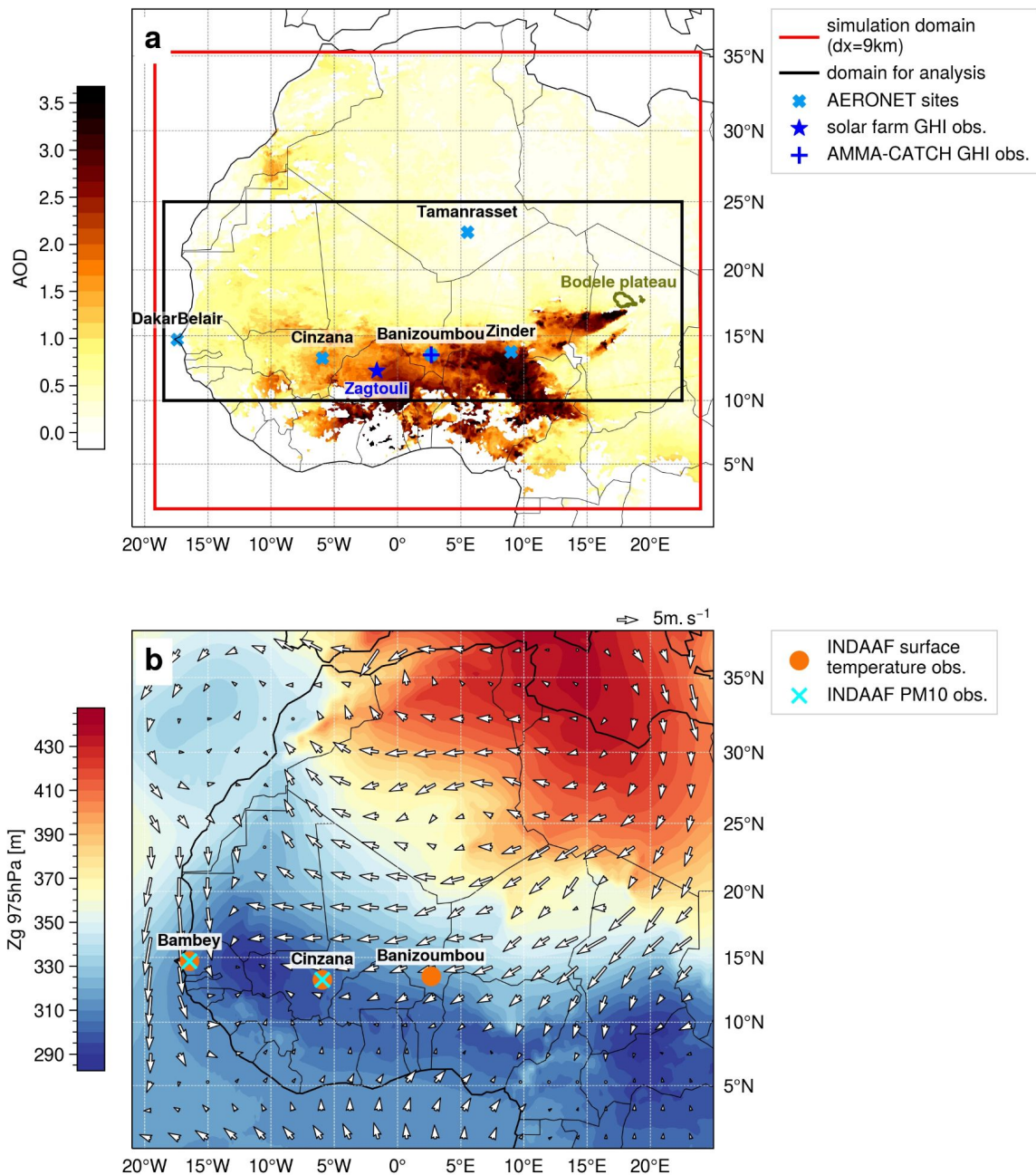
140 **2.1. Case study**

141

142 The case study is a dust event that occurs in West Africa from March 26th-00 UTC to April
143 2nd-00 UTC, 2021, i.e., during the dry season. High dust emissions occur at the Bodele
144 Depression (Chad), the plume being then transported westward. The dust plume reached its
145 maximum intensity in terms of AOD and dust concentration over West Africa, and in
146 particular over the Zagtouli solar farm (Burkina-Faso, Fig. S1), on March 30th. The event
147 was also chosen because it was not predicted in the solar forecast currently implemented for
148 the Zagtouli solar farm, leading to solar forecast errors during the passage of the dust plume
(Clauzel et al., 2024).

149

150 Figure 1 illustrates that this event is characterised by a strong Harmattan flow, with surface
151 winds from the South/South-West sweeping across the Bodele Depression (Chad), where
152 the potential for desert dust emissions is very high (Prospero et al., 2002; Washington et al.,
153 2006). Additionally, this event is characterised by a westward flow between Chad and the
154 Atlantic coast, which facilitates the transportation of the dust plume. Fig. 1a shows
155 MODerate-resolution Imaging Spectroradiometer (MODIS) satellite observations of the AOD,
156 identifying the initial dust source area on the Bodele Depression, as well as the westward
157 movement of the plume. This event is characteristic of the West African dry season
158 climatology, with a dominant Harmattan flow as described in the introduction. Figure S1
159 provides further insight into the dust plume transport during the case study.



160
 161 **Figure 1** - a) Mean aerosol Optical Depth at 550nm from MODIS satellite observations over
 162 the period 28 March-00 UTC to 02 April-00 UTC 2021. The Global Horizontal Irradiance
 163 (GHI) observations and AERONET aerosol measurement network, introduced in 2.4, are
 164 presented, as well as the boundaries of the simulated domain (red rectangle) and the area of
 165 interest for analysis (black rectangle). b) Mean synoptic conditions of the geopotential height
 166 (Zg) at 975hPa and the 10m-wind (white arrows - in m/s) over the period 28 March-00 UTC
 167 to 02 April-00 UTC 2021 from ERA5 reanalysis. The surface temperature and aerosol
 168 concentration observations from the INDAAF network, introduced in 2.4, are presented.

169

170

2.2. Modelling tools

171

172

In order to reproduce a dust event during the dry season in West Africa, the WRF-CHIMERE coupled model is selected as it has previously demonstrated favourable performance in

173 similar studies such as those conducted by Briant et al. (2017) and Menut (2023). The
 174 technical details of this coupled model are provided below.

175

176 **2.2.1. WRF model**

177 The meteorological Weather and Research and Forecasting model (WRF) model version
 178 3.7.1 is taken for compatibility with the CHIMERE coupling procedure. It is used in its non-
 179 hydrostatic configuration (Skamarock et al., 2008) and is forced at the boundaries of the
 180 domain every hour by the meteorological reanalysis data of ERA5 (ECMWF) provided on a
 181 regular 0.25° x 0.25° grid.

182 The model is run with a 9 km horizontal resolution, a 45s integration time step and 50
 183 vertical levels, from the surface to 50 hPa. The updated Rapid Radiative Transfer Model
 184 (RRTMG) radiation scheme (Iacono et al., 2008), which is mandatory for the aerosol optical
 185 properties feedback, is employed for both long- and short-wave radiations. Additionally, the
 186 Thompson aerosol-aware microphysics scheme (Thompson and Eidhammer, 2014) is
 187 applied. The Yonsei University planetary boundary layer's surface layer scheme (Hu et al.,
 188 2013) is also used, and the cumulus parameterisation is based on the Grell-Freitas scheme
 189 (Arakawa, 2004). The Revised MM5 surface layer scheme (Jiménez et al., 2012) is
 190 employed, while the Noah-MP Land Surface Model (Niu et al. 2011) is implemented for the
 191 land surface physics scheme.

192

193 **2.2.2. CHIMERE model**

194 The chemistry-transport model CHIMERE version v2020r3 (Menut et al., 2021) is used in
 195 conjunction with the WRF model. Both models have a 9 km horizontal grid. The CHIMERE
 196 model has 30 pressure-dependent vertical levels from the surface up to 200 hPa, with a first
 197 layer thickness of 3 hPa. The model is configured for dust-only, with no chemistry and only
 198 considering dust aerosols (details in section 2.3). The threshold friction velocities for dust
 199 emission are estimated using the Shao and Lu scheme (2000) and the 6-km spatial
 200 resolution GARLAP (Global Aeolian Roughness Lengths from ASCAT and PARASOL)
 201 dataset from Prigent et al. (2012). Mineral dust emission fluxes were calculated employing
 202 the Alfaro and Gomes (2001) scheme on 10 aerosol size bins ranging from 0.01 to 40 µm.
 203 The Fécan et al. (1999) parametrization is employed to account for the inhibitory effect of
 204 soil moisture on dust emission. Dry deposition is treated as described in Zhang et al. (2001).
 205 Wet scavenging for aerosol is computed following the Willis and Tattelman scheme (1989).
 206 The CHIMERE model includes the Fast-JX module, version 7.0b (Wild et al., 2000; Bian et
 207 al., 2002) for the calculation of radiative processes. It considers the radiative properties for
 208 each aerosol species and each aerosol size bin independently to compute the aerosol
 209 optical depths, the single scattering albedo and the aerosol asymmetry factor. More details
 210 on the dust aerosol radiative properties are given in Tables S1 and S2. Finally, we test three
 211 different initial and boundary condition datasets for mineral dust load (see 2.2.3).

212

213 **Table 1 - Parameterizations used in WRF and CHIMERE**

WRF	
microphysics	Thompson aerosol-aware (Thompson and Eidhammer, 2014)
radiation	RRTMG scheme for LW and SW (Iacono et al., 2008)

land surface	Noah-MP land surface scheme (Niu et al., 2011)
planetary boundary layer	Yonsei University scheme (Hu et al., 2013)
surface layer	Revised MM5 surface layer scheme (Jimenez et al., 2012)
cumulus	Grell-Freitas scheme (Arakawa, 2004)
CHIMERE	
threshold friction velocities	Shao and Lu (2000) scheme
soil moisture	Fécan et al. (1999) scheme
dust emission fluxes	Alfaro and Gomes (2001) scheme
radiative processes	Fast-JX model, version 7.0b (Wild et al., 2000; Bian et al., 2002)
aerosol size distribution bins (diameters in μm)	0.010 - 0.022
	0.022 - 0.048
	0.048 - 0.107
	0.107 - 0.235
	0.235 - 0.516
	0.516 - 1.136
	1.136 - 2.500
	2.500 - 5.000
5.000 - 10.00	
10.00 - 40.00	

214

215

2.2.3. Dust aerosol initial and boundary condition datasets

216 In this study, the uncertainty in the solar estimate associated with the initial and boundary
 217 conditions of the dust aerosol load is evaluated. Three datasets were used: a climatology
 218 derived from the Global Ozone Chemistry Aerosol Radiation and Transport (GOCART,
 219 Ginoux et al., 2001), the Modern-Era Retrospective analysis for Research and Applications
 220 Version 2 (MERRA2) reanalysis (Gelaro et al., 2017) and the CAMS reanalysis (Inness et
 221 al., 2019).

222 The GOCART climatology is provided with the distribution of the CHIMERE model. It is a
 223 monthly climatology on a coarse horizontal grid ($2^\circ \times 2.5^\circ$), which is corrected by applying a
 224 factor of 0.3 as in Vautard et al. (2005).

225 The MERRA2 reanalysis combines the Goddard Earth Observing System (GEOS) and
 226 GOCART models, which are online coupled and implemented with a data assimilation
 227 system. It has a 3-hour temporal resolution and is presented on a $0.5^\circ \times 0.635^\circ$ horizontal
 228 grid. The observational data considered in the data assimilation process are AOD satellite
 229 observations from MODIS, Advanced Very High Resolution Spectroradiometer (AVHRR),
 230 Multi-angle Imaging SpectroRadiometer (MISR) and ground observations from the AEROSOL
 231 RObotic NETwork (AERONET).

232 The CAMS reanalysis was constructed using 4DVar data assimilation in ECMWF's
 233 Integrated Forecast System (IFS). It has a temporal resolution of 3 hours and is computed
 234 on a regular 0.75° horizontal grid. The AOD data from the Visible Infrared Imaging
 235 Radiometer Suite (VIIRS), the MODIS and the Infrared Atmospheric Sounding Interferometer
 236 (IASI) satellite observations are used as observational information in the data assimilation
 237 process. The version 48R1 of CAMS is used in this study.

238 These three dust aerosol initial and boundary datasets differ in type (climatological or
 239 reanalysis), in horizontal, vertical and temporal resolution, and in the resolution and range of
 240 their aerosol size distribution. While GOCART has the highest number of aerosol classes
 241 with 7 bins, CAMS covers a wider size spectrum despite a lower size resolution with only 3
 242 classes. MERRA2 has an intermediate resolution with 5 classes, but covers a smaller
 243 particle size spectrum than CAMS. The CHIMERE model pre-processes these dust aerosol
 244 size distributions by applying a transfer coefficient δ to compute the dust aerosol
 245 concentration on the 10 aerosol size bin defined for the simulations :

$$c_j = \sum_i \delta_{i,j} \times c_i \quad (1)$$

246 where c_i is the dust aerosol concentration of the i^{th} size bin from the initial and boundary
 247 condition dataset considered, c_j is the dust aerosol concentration of the j^{th} size bin in the
 248 CHIMERE simulation, and $\delta_{i,j}$ is the transfer coefficient. This transfer coefficient is derived
 249 as :

- 250 - $\delta_{i,j} = 0$ if the i^{th} size bin from the initial and boundary condition dataset is found to be
 251 wholly outside the j^{th} size bin in the CHIMERE simulation;
- 252 - $\delta_{i,j} = 1$ if the i^{th} size bin from the initial and boundary condition dataset is wholly
 253 encompassed by the j^{th} size bin in the CHIMERE simulation;
- 254 - $\delta_{i,j} = \frac{\log(r_{j,max}) - \log(r_{j,min})}{\log(R_{i,max}) - \log(R_{i,min})}$ if the i^{th} size bin from the initial and boundary condition
 255 dataset wholly encompasses the j^{th} size bin in the CHIMERE simulation;
- 256 - $\delta_{i,j} = \frac{\log(R_{i,max}) - \log(r_{j,min})}{\log(R_{i,max}) - \log(R_{i,min})}$ if the i^{th} size bin from the initial and boundary condition
 257 dataset partially overlaps the j^{th} size bin in the CHIMERE simulation, but extends
 258 below the start of this size bin;
- 259 - $\delta_{i,j} = \frac{\log(r_{j,max}) - \log(R_{i,min})}{\log(R_{i,max}) - \log(R_{i,min})}$ if the i^{th} size bin from the initial and boundary condition
 260 dataset partially overlaps the j^{th} size bin in the CHIMERE simulation, but extends
 261 beyond the end of this size bin;

262 where $R_{i,min}$ and $R_{i,max}$ are respectively the radius of the lower and upper limit of the i^{th} size
 263 bin from the initial and boundary condition dataset, and $r_{j,min}$ and $r_{j,max}$ are respectively the
 264 radius of the lower and upper limit of the j^{th} size bin in the CHIMERE simulation.

265
 266 For the sake of simplicity, throughout this article, we will refer to the WRF-CHIMERE
 267 simulations runned with the GOCART, the MERRA2, and the CAMS dust aerosol initial and
 268 boundary conditions as *wrf_chimere-G*, *wrf_chimere-M*, and *wrf_chimere-C* simulations
 269 respectively.

270 Table 2 summarises the characteristics of the three dust aerosol datasets and their
 271 associated size distributions.

272

273 **Table 2.** Summary of the characteristics of the dust initial and boundary condition products.

	GOCART	MERRA2	CAMS
type	climatology	reanalysis	reanalysis
temporal resolution	monthly	3h	3h
vertical levels	20	72	60
horizontal resolution (lat x lon)	2°x2.5°	0.5°x0.635°	0.75°x0.75°
dust aerosol size distribution (radius in µm)	0.20 - 0.36 µm	0.1 - 1.0 µm	0.03 - 0.55 µm
	0.36 - 0.60 µm	1.0 - 1.8 µm	0.55 - 0.90 µm
	0.60 - 1.20 µm	1.8 - 3.0 µm	0.90 - 20.00 µm
	1.20 - 2.00 µm	3.0 - 6.0 µm	
	2.00 - 3.60 µm	6.0 - 10.0 µm	
	3.60 - 6.00 µm		
	6.00 - 12.00 µm		

274

275 **2.3. Modelling strategy**

276 The domain of simulation extends from 2° to 35°N and from 19°W to 24°E, as illustrated by
 277 the red box in Figure 1b. The domain is large enough to represent the primary atmospheric
 278 flows, including the Harmattan North/North-West flow and the monsoon South flow, as well
 279 as the transport of the emitted aerosol plumes. A horizontal resolution of 9 km has been
 280 selected in order to ensure that the grid ratio is approximately 3 with the ERA5
 281 meteorological forcing. This choice is also motivated by the a priori intention to achieve a
 282 resolution higher than that of previous CHIMERE simulations performed in this region and
 283 compared to the operational solar forecast model used for the Zagtoui solar farm, which are
 284 based on global forecast models (see 2.4.1). The CHIMERE model is configured in a “dust
 285 only” model, which models only the mineral dust type. This hypothesis is supported for this
 286 dust case study by Fig. S2, as desert dust is the dominant aerosol during the event,
 287 particularly above 10°N. This hypothesis is also reinforced by the dust optical depth (DOD)
 288 to AOD ratio derived from the CAMS reanalysis, which exceeds 80% during this case study
 289 and for the domain of interest (not shown). It is notable that biomass burning, which
 290 represents the other principal aerosol source in this region, is no longer a significant
 291 contributor to aerosol levels at that time of the year (Evans et al., 2018).

292 The WRF and CHIMERE models are coupled online through the OASIS3 MCT coupler. A
 293 two-way coupling strategy is selected, in which WRF sends meteorological variables to
 294 CHIMERE which in turn exchanges aerosol information such as AOD, Single Scattering
 295 Albedo (SSA) and Asymmetry Factor. This coupling strategy imposes most of the WRF
 296 parameterisations. The exchange frequency is set to 15 minutes. The WRF model computes

297 fields on 50 levels, which are linearly interpolated over the 30 CHIMERE vertical levels via
298 the OASIS coupler. The coupling includes the feedbacks of aerosol-radiation interactions
299 (ARI, direct aerosol effect) and aerosol-cloud interactions (ACI, indirect aerosol effects)
300 simultaneously.

301 The simulation starts on March 14th-00 UTC and ends on April 2nd-00 UTC, 2021. The first
302 two weeks served as the spin-up period. The simulation outputs are analysed for the period
303 of March 28th-00 UTC to April 2nd-00 UTC, which corresponds to the passage of the
304 dust plume in the Sahel region, in particular around the Zagtouli solar farm in Burkina Faso.
305 Four simulations were conducted: a meteorological simulation using WRF model alone, and
306 dust simulations with the coupled WRF-CHIMERE models using as initial and boundary
307 conditions the GOCART climatology, the MERRA2 reanalysis and the CAMS reanalysis. The
308 simulation using only WRF allows for the evaluation of the impact of taking into account dust
309 aerosols in estimating solar irradiance. This is compared to the other three simulations,
310 which are also used to evaluate the uncertainties associated with the choice of the aerosol
311 initial and boundary condition dataset. A domain of interest, spanning 10°N to 25°N (Fig. 1a),
312 was selected for analysis and comparisons. This choice was guided by the dust plume
313 trajectory (Fig. S1) and the “dust only” hypothesis (Fig. S2).

314

315 **2.4. Evaluation datasets**

316 This section presents the local and regional data that are employed in the evaluation of the
317 simulations.

318

318 **2.4.1. GHI**

319 The Global Horizontal Irradiance (GHI) is the total shortwave irradiance from the Sun on a
320 horizontal surface on Earth. It is the sum of direct irradiance, which takes into account the
321 solar zenith angle, and diffuse horizontal irradiance. It is measured in $W.m^{-2}$ for the
322 wavelength range 0.3 - 3.0 μm .

323

324 The national electricity company of Burkina-Faso, Sonabel, operates a solar farm in Zagtouli
325 (12.31°N;1.64°W; Fig. 1a), approximately 15 km west of the capital, Ouagadougou. It has an
326 installed capacity of 34 MWp and contributes up to 4% of Burkina Faso's annual electricity
327 production. Ground GHI measurements from pyranometers are available at a temporal
328 resolution of 15 minutes for the Zagtouli solar plant and undergo pre-processing to ensure
329 quality control. This involves removing outliers and days with missing data, visually checking
330 the consistency of the measured values and selecting data corresponding to production
331 hours (positive values for solar irradiance at the top of the atmosphere). Operational GHI
332 forecasts for this solar farm are computed by the French company Steadysun. These
333 forecasts are based on a multi-model, multi-member and multi-mesh grid aggregation, which
334 is derived from the NCEP Global Ensemble Forecast System and the ECMWF Integrated
335 Forecast System (Clauzel et al., 2024).

336 In-situ measurements of GHI from pyranometers (Fig. 1a) are also available at a 15-minutes
337 temporal resolution for the Banizoumbou (Niger) surface station, installed as part of the
338 AMMA-CATCH observatory (Analyse Multidisciplinaire de la Mousson Africaine - Couplage
339 de l'Atmosphère Tropicale et du Cycle Hydrologique, AMMA-CATCH (2005)).

340 The two measurement sites were selected because they are the only locations where GHI
341 observations have been made available along the dust plume transport for the case study,
342 with the Zagtouli power station being one of the first large solar farms in West Africa and the
343 AMMA-CATCH observatory being the only one to offer continuous GHI measurements for
344 the region and period of interest.

345

346 The CAMS gridded solar radiation dataset (CAMS solar radiation services v4.6, Schroedter-
347 Homscheidt et al., 2022), based on the Heliosat-4 method (Qu et al., 2017), provides several
348 variables related to solar irradiance, such as clear-sky and all-sky GHI. It has a horizontal
349 resolution of $0.1^\circ \times 0.1^\circ$ and provides data every 15 minutes. The clear sky model includes
350 aerosols through the CAMS chemical transport model (Inness et al., 2019), which integrates
351 data assimilation of AOD and is coupled online to a numerical weather prediction model.
352 Cloud information for the all-sky model is derived from MeteoSat Second Generation (MSG)
353 satellite observations using the AVHRR Processing scheme Over cLOUDs, Land and Ocean
354 (APOLLO) Next Generation cloud processing scheme (Klüser et al., 2015). The dataset was
355 selected for comparison with the simulations as it integrates a description of aerosol
356 processes. While Yang and Bright (2020) and Sawadogo et al. (2023) show that it is the best
357 performing product for estimating surface solar irradiance in the West African region among
358 several satellite-based gridded irradiance products, this dataset still has a negative bias of
359 about 10% for all-sky solar irradiance estimates at desert stations in North Africa (CAMS
360 solar radiation regular validation report, Lefèvre, 2022).

361

362

2.4.2. Surface temperature

363 In-situ surface temperature measurements are available for three stations of the
364 International Network to study Deposition and Atmospheric composition in Africa (INDAAF) :
365 Banizoumbou (Niger, 13.54° N, 2.66° E, 6.2m above surface; Rajot et al, 2010a; Marticorena
366 et al, 2010; Kaly et al., 2015), Cinzana (Mali, 13.28° N, 5.93° W, 2m above surface; Rajot et
367 al, 2010b; Marticorena et al, 2010; Kaly et al., 2015) and Bambey (Senegal, 14.70° N,
368 16.47° W, 5.2m above surface; Marticorena et al, 2021a) (Fig. 1b). The measurement sites
369 were selected since they are almost aligned around $13\text{-}15^\circ$ North, which represents the main
370 pathway of Saharan and Sahelian dust towards the Atlantic Ocean during the case study.
371 The ERA5 atmospheric reanalysis (Hersbach et al., 2020) provides spatially continuous
372 hourly values of surface temperature at 2 metres and has a horizontal resolution of $0.25^\circ \times$
373 0.25° .

374

375

2.4.3. Aerosol

376 The INDAAF network also provides data on aerosol concentration through ground
377 measurements of PM_{10} , i.e. the concentration of atmospheric particles having an
378 aerodynamic diameter less than $10\ \mu\text{m}$. For this case study, hourly PM_{10} measurements are
379 available for two stations (Fig. 1b): Cinzana (Rajot et al, 2010c; Marticorena et al, 2021; Kaly
380 et al, 2015) and Bambey (Marticorena et al, 2021b).

381 The CAMS atmospheric reanalysis (Inness et al., 2019) is also used to evaluate regional
382 surface PM_{10} concentration and AOD. It provides 3-hourly data with a horizontal resolution of
383 $0.75^\circ \times 0.75^\circ$, with a surface layer thickness of 2.4 hPa.

384

385 Local ground measurements of AOD are retrieved from the AErosol RObotic NETwork level
386 1.5 dataset (AERONET, Holben et al., 1998; Giles et al., 2019). AOD is calculated from sun
387 photometer recordings, along with Ångström Exponent, and is only available during clear sky
388 conditions in daylight hours, with a resolution of 1 minute. The AOD at 400 nm simulated
389 with the WRF-CHIMERE model is converted to 440 nm for comparison with AERONET,
390 using the Ångström formula :

$$\frac{AOD_{\lambda}}{AOD_{\lambda_0}} = \left(\frac{\lambda}{\lambda_0} \right)^{-\alpha} \quad (2)$$

391 where AOD_{λ} is the AOD at the desired wavelength, $\lambda=440\text{ nm}$ here ; AOD_{λ_0} is the AOD at
 392 the wavelength simulated in the model, $\lambda_0=400\text{ nm}$ here ; α is the Ångström exponent,
 393 derived from the simulated AOD at different wavelengths and here given for the range from
 394 400 nm to 600 nm.

395

396 AERONET also provides an aerosol size distribution dataset estimated through inversion of
 397 the photometers data, as described in Dubovik and King (2000). The algorithm for inversion
 398 provides a volume particle size distribution for 22 bins, which are logarithmically distributed
 399 for radii between 0.05 μm and 15 μm . For comparison with the modelled aerosol size
 400 distribution, this distribution is interpolated on the CHIMERE simulated aerosol size
 401 distribution which is composed of 10 bins ranging from 0.01 μm to 40.00 μm in diameter (see
 402 Table 1). Given that the coarsest bin (10.00-40.00 μm) is at the limit of the capabilities of the
 403 inversion method, and the two thinnest bins (0.010-0.022 μm and 0.022-0.048 μm) are out of
 404 the range of the inversion product, the AERONET dataset size sections are interpolated on
 405 the CHIMERE size sections ranging from 0.048 to 10.0 μm . Consequently, only comparisons
 406 between the three simulations can be made for the three size sections which are out of the
 407 range of AERONET product. The column aerosol volume size distribution simulated by the
 408 model is calculated for each bin “ i ” as in Menut et al. (2016) :

$$\frac{dV(r_i)}{d \ln(r_i)} = \sum_{k=1}^{nlevels} \frac{m_{k,r_i} \times \Delta z_k}{\rho_{dust} \times \ln(r_{i,max}/r_{i,min})} \quad (3)$$

409 where r_i is the mean mass median radius (in μm) and $r_{i,min}$ and $r_{i,max}$ the boundaries of the
 410 i^{th} bin. m_{k,r_i} is the dust aerosol mass concentration (the mass of aerosol in one cubic metre
 411 of air, in $\mu\text{g} \cdot \text{m}^{-3}$). ρ_{dust} is the dust aerosol density (the mass of the particle in its own volume,
 412 $\rho_{dust}=2300\text{ kg} \cdot \text{m}^{-3}$). Δz_k is the model layer thickness (in metres), for a total of n levels (here
 413 30 vertical levels).

414

415 The locations of the five AERONET sites used for comparison in this study are illustrated in
 416 Figure 1a.

417

418 The spatially continuous AOD is also derived from level 2 aerosol products of MODIS Terra
 419 and Aqua satellites (combined Dark Target, Deep Blue AOD at 0.55 micron, Collection 6.1,
 420 Platnick et al., 2015). It provides a measure of the AOD at 550 nm during daytime for clear
 421 sky conditions, with a spatial resolution of 10 km. To compare simulated AOD from WRF-
 422 CHIMERE models with AOD from MODIS, the former is converted from 600 nm to 550 nm.
 423 The conversion is performed using the Ångström formula (eq. 2).

424

425 Table 3 provides a general overview of the data used to evaluate the simulations in this
 426 study.

427

428 **Table 3** - Summary of data used to evaluate the simulations.

product	type	resolution
---------	------	------------

	Zagtouli solar farm monitoring system	pyranometer GHI measurement	local
GHI	AMMA-CATCH observational network	pyranometer GHI measurement	local
	CAMS gridded solar radiation	atmospheric reanalysis	0.01°x0.01°
	INDAAF network	ground measurements	local
temperature	ERA5	atmospheric reanalysis	0.25°x0.25°
	INDAAF network	ground measurements	local
PM₁₀	CAMS (v48R1, EAC4)	atmospheric reanalysis	0.75°x0.75°
Aerosol Size Distribution	AERONET network	inversion product	local
	AERONET network	sunphotometer ground measurements	local
Aerosol Optical Depth	MODIS	satellite observations	10km

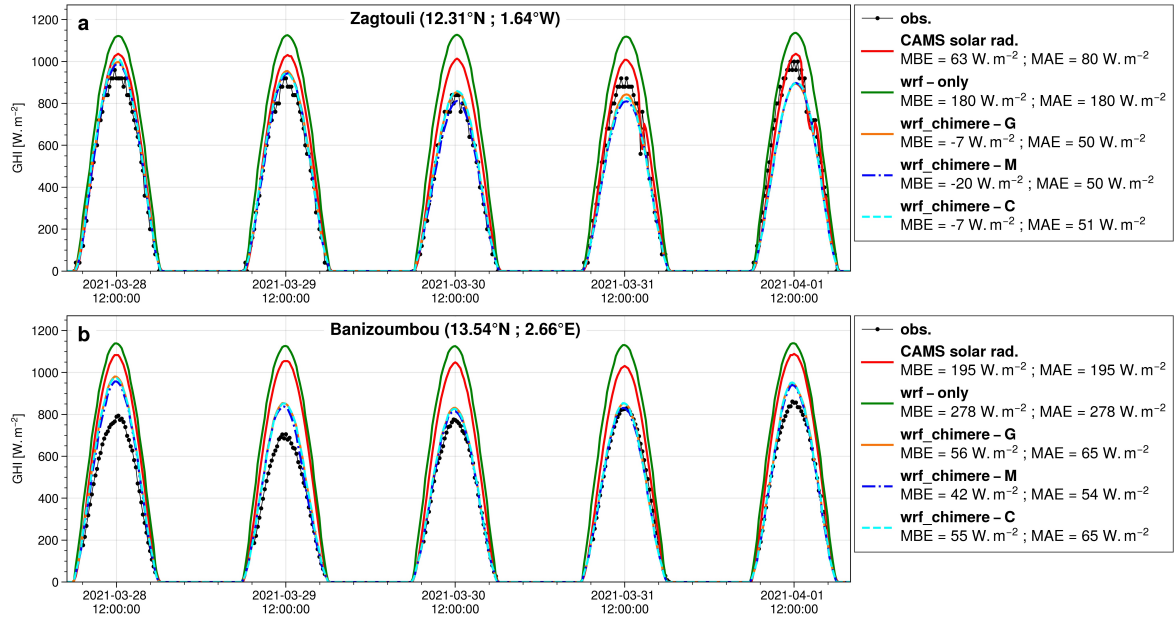
429

430 **3. Results**

431 The analysis starts by assessing the errors and uncertainties associated with the dust
 432 aerosol initial and boundary condition dataset employed to estimate the variables of interest
 433 for solar production, i.e. GHI and surface temperature. Subsequently, we investigate the
 434 potential causes of these uncertainties by evaluating the AOD, aerosol size distribution, and
 435 surface aerosol concentration (PM₁₀), as well as by examining mineral dust emissions and
 436 the flux of these aerosols at the boundaries of the domain. The metrics used to assess the
 437 quality of the simulations are described in Supplementary Materials.

438

439 **3.1. GHI**



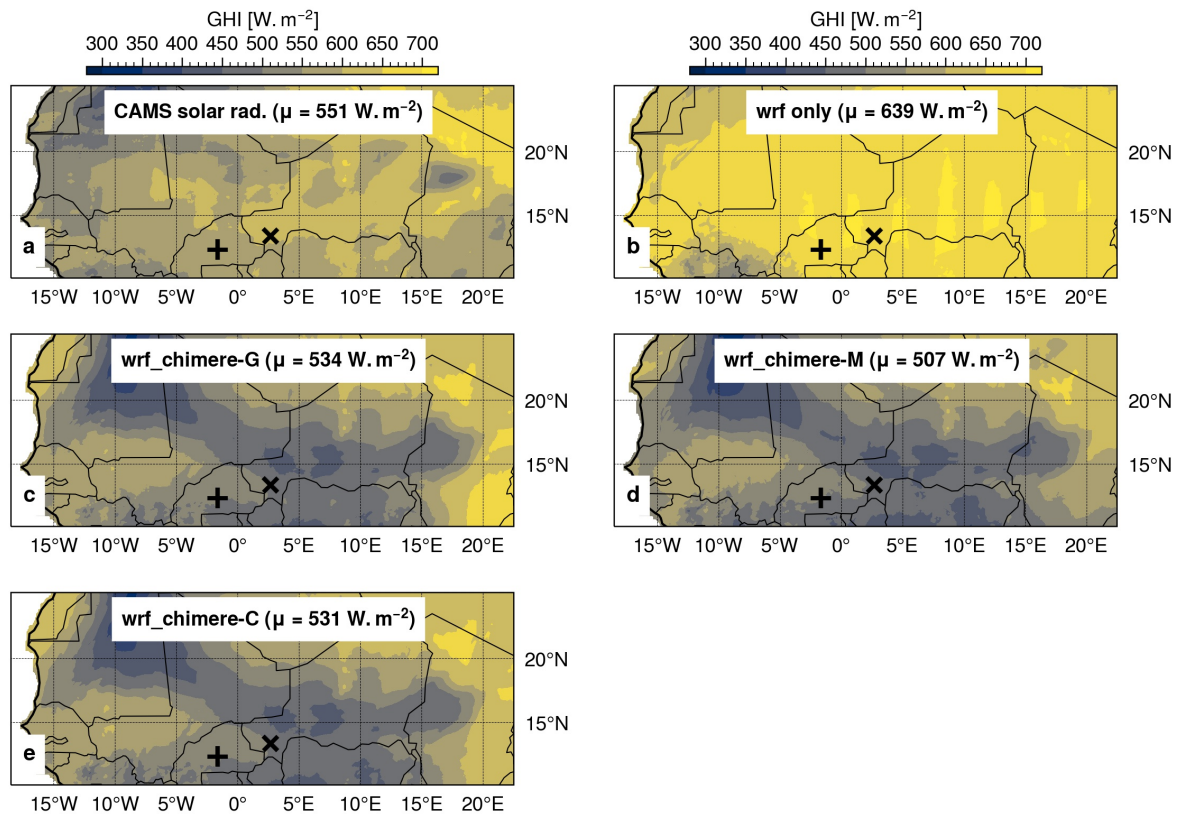
440
 441 **Figure 2** - Local comparison of CAMS gridded solar radiation product and simulated GHI
 442 against a) the Zagtouli solar farm observations and b) the Banizoumbou AMMA-CATCH
 443 observations. *wrf_chimere-G*, *wrf_chimere-M* and *wrf_chimere-C* refer to the WRF-
 444 CHIMERE simulations using GOCART, MERRA2 and CAMS as dust aerosol initial and
 445 boundary condition dataset respectively.

446
 447 In Fig. 2, the local evaluation demonstrates the effect of taking into account dust aerosol for
 448 GHI estimation with the WRF-CHIMERE coupling over the WRF meteorological model
 449 alone. The coupling reduces the MAE by a factor of 3.6 at Zagtouli and by a factor of 4.6 at
 450 Banizoumbou on average. The simulations accurately represent the reduction in GHI
 451 intensity caused by the dust plume at both stations. However, the reduction persists
 452 compared to the observations at Zagtouli. At Banizoumbou, the simulations overestimate
 453 GHI at the beginning and end of the case study.

454 Figure 2 also indicates that the CAMS gridded solar radiation product fails to fully reproduce
 455 the dust event, with only a small reduction in GHI during the passage of the dust plume and
 456 an intermediate MAE between the WRF only and the WRF-CHIMERE simulations. This point
 457 serves to highlight the advantages of using a regional model in comparison to a global
 458 product for the simulation of dust conditions and the estimation of solar irradiance.

459 Furthermore, the uncertainty in GHI estimation related to the choice of the dust aerosol initial
 460 and boundary condition dataset is limited, particularly when compared to the errors. This is
 461 evidenced by the fact that the mean standard deviation between the three WRF simulations
 462 is only 7% of the average MAE of these simulations at Zagtouli, and only 5% at
 463 Banizoumbou.

464



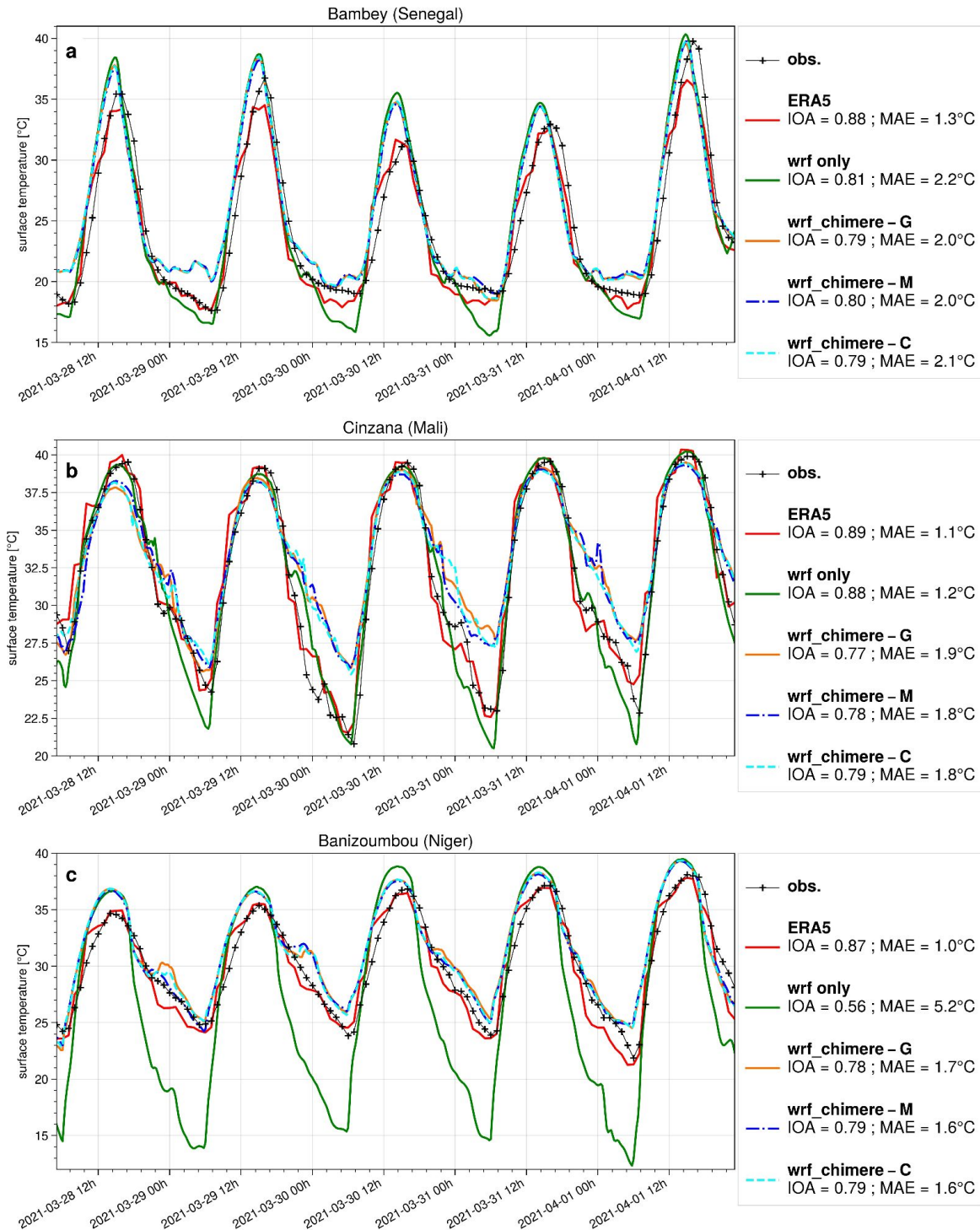
465
 466 **Figure 3** - Mean day-time GHI during the period of 28 March-00 UTC to 02 April-00 UTC
 467 2021 as estimated by a) the CAMS gridded solar radiation dataset, b) the WRF only
 468 simulation, and the WRF-CHIMERE simulations with c) GOCART, d) MERRA2 and e)
 469 CAMS as dust aerosol initial and boundary condition dataset; + is the Zagtoui solar farm
 470 and x is the Banizoumbou site. μ is the mean GHI estimates over the domain.

471
 472 The regional comparison presented in Fig. 3 provides more insight into the impact of
 473 incorporating dust on GHI estimation with the WRF-CHIMERE coupling, when compared to
 474 the WRF meteorological model alone. As anticipated the WRF-only simulation has the
 475 highest GHI estimates. The WRF-CHIMERE simulations indicate that dust aerosols reduce
 476 the mean GHI estimation by approximately $115 W . m^{-2}$ (-18%) as compared to the WRF-only
 477 simulation, while the CAMS gridded solar radiation global product shows a reduction of
 478 $88 W . m^{-2}$ (-14%). The three WRF-CHIMERE simulations exhibit identical regional patterns,
 479 with lower mean GHI values observed on the dust plume trajectory from the Bodele
 480 Depression to the West, and also in the South Atlas region. In contrast, the CAMS gridded
 481 solar radiation dataset does not show this regional pattern, which may indicate that this
 482 global product does not fully capture the dust event.

483 Furthermore, the uncertainty in GHI estimation associated with the choice of the dust aerosol
 484 initial and boundary conditions dataset is limited, particularly when compared to the changes
 485 brought by the taking of dust aerosol into account. Indeed, the standard deviation between
 486 the three WRF-CHIMERE simulations represents only 5% of the mean difference between
 487 these three simulations and the WRF-only simulation without dust.

488
 489

3.2. Temperature



490
 491 **Figure 4** - Local comparison of ERA5 and simulated surface temperature with the INDAAF
 492 observations for a) Bambey (Senegal), b) Cinzana (Mali) and c) Banizoumbou (Niger)
 493 measurement sites. *wrf_chimere-G*, *wrf_chimere-M* and *wrf_chimere-C* refer to the WRF-
 494 CHIMERE simulations using GOCART, MERRA2 and CAMS as dust aerosol initial and
 495 boundary condition dataset respectively. *IOA* is the Indicator of Agreement and *MAE* is the
 496 Mean Absolute Error.

497
 498 Figure 4 illustrates the contrasting outcomes of taking into account dust aerosols into the
 499 WRF-CHIMERE coupling in comparison to the WRF meteorological model alone for the

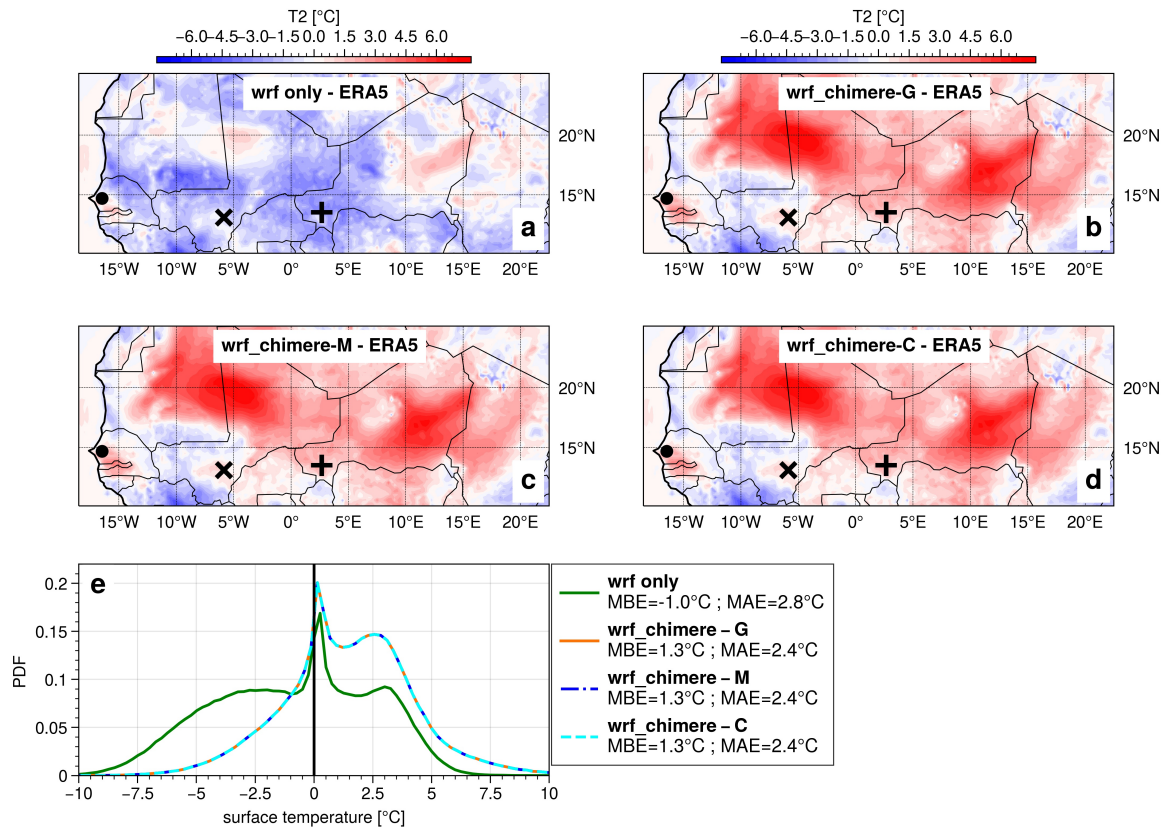
500 estimation of surface temperature. At Bambey (Fig. 4a), which is far from the dust source
501 areas, the coupling has no effect on daytime temperatures but does affect night-time
502 temperatures. The WRF-CHIMERE and WRF-only simulations have IOA and MAE of the
503 same order of magnitude. At Cinzana (Fig. 4b), the WRF-only simulation performed better,
504 with a MAE 0.6°C lower than the coupled simulations, especially for night-time temperatures
505 but also for estimating the daily temperature peak. Finally, at Banizoumbou (Fig. 4c), which
506 is near the dust source areas, the coupling leads to a significant improvement in surface
507 temperature estimation, with an IOA of approximately 0.79 compared to 0.56 for the WRF-
508 only simulation and a MAE reduced by around 3.6°C. The impact of dust aerosols on
509 temperature is particularly pronounced at night-time. However, dust also affects the daily
510 temperature peak, with a reduction of 1.1°C of the daily maximum temperature observed on
511 the 30th of March.

512 Depending on the position of the measurement station, the results show a contrast, with a
513 significant improvement with the model coupling close to the source zones at Banizoumbou.
514 However, this improvement is reversed with increasing distance at Cinzana. This suggests
515 errors in the simulation of the transport of the dust plume from the source zones (Bodele
516 Depression) towards the West. Overall, the main differences between WRF only and WRF-
517 CHIMERE coupled simulations occur at night time when there is no solar production. These
518 differences highlight the warming effect due to the dust aerosol interaction with the longwave
519 earth radiation.

520 In general, the uncertainty associated with the choice of the dust aerosol initial and boundary
521 condition dataset for the WRF-CHIMERE simulations is negligible compared to the errors in
522 temperature estimation or the difference with the WRF-only simulation.

523 The value of the ERA5 reanalysis for surface temperature evaluation is also reinforced in
524 Fig. 4, since it shows the lowest MAE and highest IOA. This dataset can therefore be
525 considered reliable for a regional evaluation of surface temperature.

526



527
 528 **Figure 5** - Mean difference in surface temperature as compared to the ERA5 reanalysis for
 529 a) the WRF only simulation, the WRF-CHIMERE simulations with b) GOCART, c) MERRA2
 530 and d) CAMS as dust aerosol initial and boundary condition dataset, during the period of 28
 531 March-00 UTC to 02 April-00 UTC 2021; the black point is the Bambey, x is the Cinzana and
 532 + is the Banizoumbou INDAAF sites. e) Probability Density Function for the differences in
 533 surface temperature between simulations and the ERA5 reanalysis.

534
 535 The regional surface temperature evaluation in Fig. 5 also reveals a contrast benefit of the
 536 coupling approach for the surface temperature estimation. While the WRF alone simulation
 537 (Fig. 5a) underestimates the surface temperature all over the domain, WRF-CHIMERE
 538 simulations are overestimating surface temperature in the dusty areas (Saharan region, Fig.
 539 5bcd). Overall, taking into account dust aerosol in the estimation of surface temperature
 540 reduces the MAE by 14% (Fig. 5e) when comparing the surface temperature estimates from
 541 simulations with the ERA5 reanalysis.

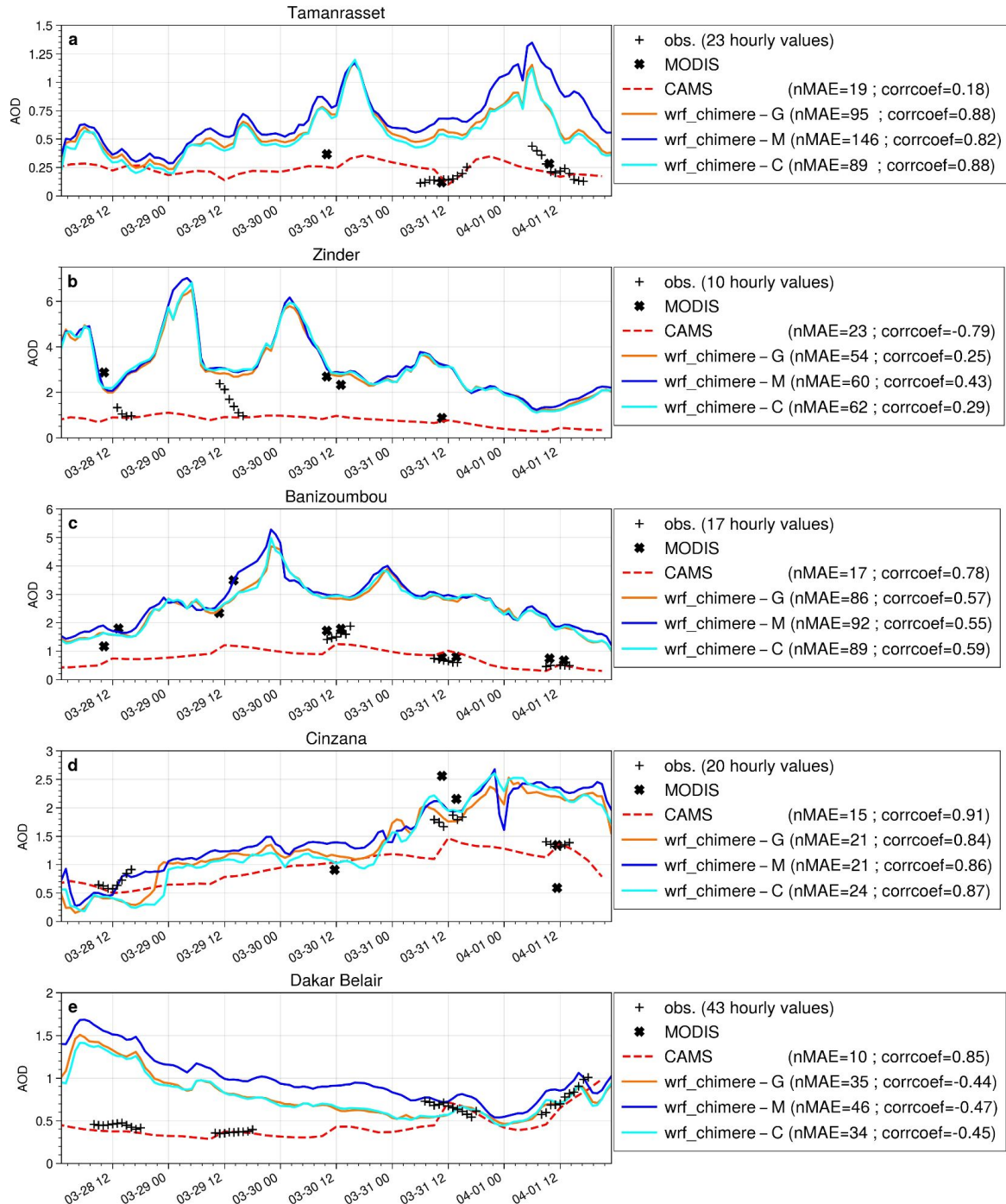
542 Furthermore, the uncertainty associated with the choice of the dust aerosol initial and
 543 boundary conditions dataset is limited. This is demonstrated by the fact that the standard
 544 deviation between the three WRF-CHIMERE simulations averaged over the period of
 545 analysis is 12% of the mean bias of those three simulations in comparison to ERA5
 546 reanalysis, and only 7% of the difference between the coupled simulations and the WRF-
 547 only simulation without dust.

548
 549 Finally, the incorporation of dust aerosol into the estimation of GHI appears to be a crucial
 550 element in this case study. However, the value of this approach is more debatable in the
 551 context of surface temperature estimation. Furthermore, the uncertainty related to the dust
 552 aerosol initial and boundary condition dataset selection is limited, particularly when

553 compared to the simulation errors, and to the differences between including dust in the
 554 simulation and not including it. The following sections will examine the simulated dust
 555 aerosol condition during the case study in order to explain the discrepancies observed in
 556 GHI and surface temperature, which are key parameters for solar production.
 557

558

3.3. Aerosol Optical Depth

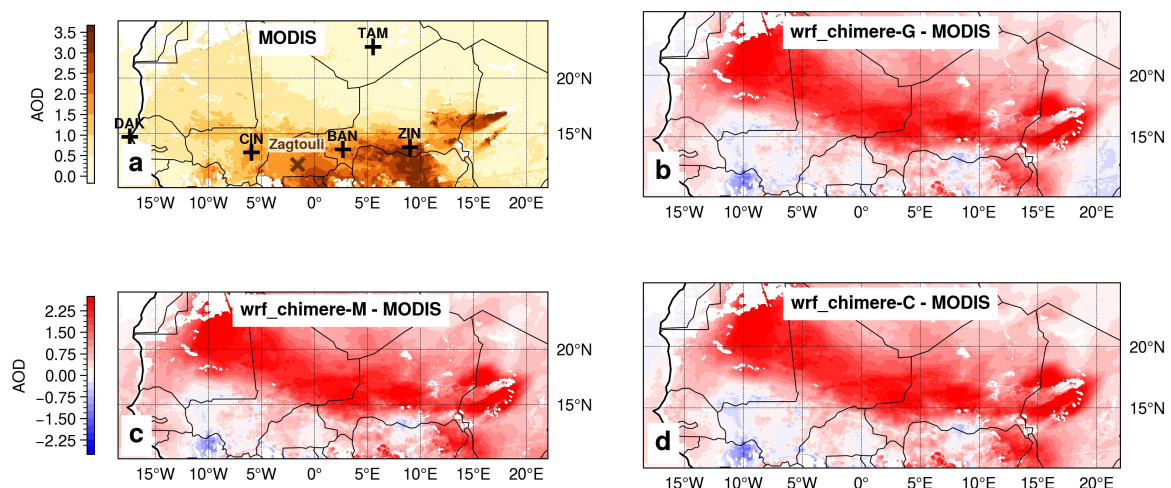


559
 560 **Figure 6** - Local comparison of simulated AOD with AERONET in-situ measurements at 440
 561 nm for a) Tamanrasset, b) Zinder, c) Banizoumbou, d) Cinzana and e) Dakar Belair stations.
 562 *wrf_chimere-G*, *wrf_chimere-M* and *wrf_chimere-C* refer to the WRF-CHIMERE simulations
 563 using GOCART, MERRA2 and CAMS as dust aerosol initial and boundary condition dataset

564 respectively; *MODIS* and *CAMS* refer to the AOD at 440 nm from the MODIS satellite
 565 observations and the CAMS atmospheric reanalysis respectively. *nMAE* is the normalised
 566 mean absolute error in % and *corrcoef* is the Pearson correlation coefficient, both derived
 567 with AERONET measurements as the reference.
 568

569 The local evaluations presented in Figure 6 reveal an overestimation of the AOD for stations
 570 close to dust sources such as Tamanrasset (Fig. 6a), Zinder (Fig. 6b) and Banizoumbou
 571 (Fig. 6c). This overestimation is more limited with increasing distance from the dust source
 572 at Cinzana (Fig. 6d) and Dakar (Fig. 6e). The order of magnitude of the dispersion between
 573 the three simulations is small when compared to the errors of the simulation in representing
 574 the observed AOD. As a consequence, the uncertainty associated with the choice of the dust
 575 aerosol initial and boundary condition dataset is limited. Overall, the AERONET AOD
 576 measurements appear to be very scarce, particularly close to the dust aerosol sources
 577 (Zinder, Tamanrasset, Banizoumbou, Cinzana). The AOD measurements are performed by
 578 sun photometers which give recording by pointing at the sun. Thus these recordings are only
 579 available during daytime and with clear sky conditions. In some cases of intense dust
 580 plumes with very high concentration, leading to strong solar radiation absorption, the sun
 581 photometers are technically limited and cannot produce any record or, sometimes, the
 582 AERONET quality control system removes them (Mueller et al., 2015 ; Giles et al., 2019).
 583 This may be the reason for the scarcity of observations in this case study, which focuses on
 584 an intense dust event, increasing the perceived overestimation of the simulations. To
 585 compensate for this, the AOD estimates from MODIS satellite observations have been
 586 added to Figure 6 to complete the data.

587 Furthermore, the CAMS reanalysis appears to be a reliable dataset for dust AOD estimation,
 588 as it has no overestimation and has the lowest *nMAE* for all sites. Although it does not
 589 reproduce the AOD dynamics close to the dust source at Tamanrasset and Zinder, it has the
 590 highest correlation coefficient for the other sites. Nevertheless, this result should be
 591 interpreted with caution, given the limited data available for calculating the dataset
 592 evaluation metrics. More research is needed to substantiate this conclusion.
 593



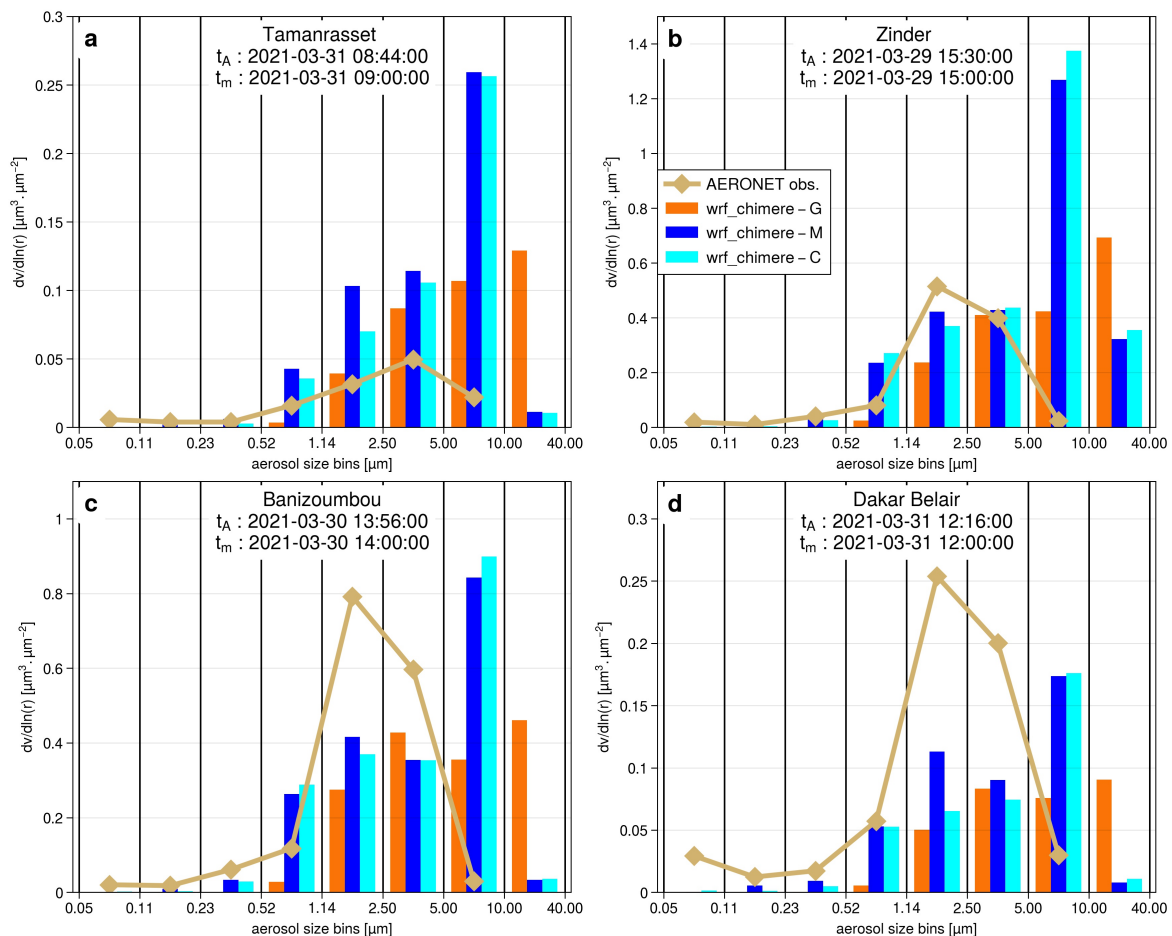
594
 595 **Figure 7** - a) Mean from March 28th-00 UTC to April 2nd-00 UTC 2021 of MODIS AOD at
 596 550 nm satellite observations; x is the Zagtoui solar farm and + corresponds to AERONET
 597 stations. For panels b, c and d, AOD at 550 nm mean differences from March 28th-00 UTC

598 to April 2nd-00 UTC 2021 between each of the WRF-CHIMERE simulations driven by
 599 GOCART, MERRA2 and CAMS, respectively, and the MODIS satellite observations.
 600

601 The AOD differences shown in Fig. 7bcd show that the simulations significantly overestimate
 602 the AOD as compared to the MODIS satellite observations, particularly in the Saharan and
 603 North Sahelian zones and in the South Atlas, with an average overestimation of +1.25
 604 between 15°N and 20°N. It is important to note that this overestimation is localised close to
 605 the desert aerosol source zones. The simulated AOD error in the Sahel zone, particularly
 606 around the Zagtouli solar power plant, is more limited with an average of +0.51 between
 607 10°N and 15°N. The mean standard deviation between the three WRF-CHIMERE
 608 simulations is only 10% of the mean error and 5% of the mean simulated AOD.
 609 Consequently the uncertainty in the AOD estimate associated with the selection of the dust
 610 aerosol initial and boundary condition dataset is small.

611 The observed overestimation of AOD by the WRF-CHIMERE simulations could be due to an
 612 overestimation of the aerosol concentration, or to an inaccurate estimation of the size
 613 distribution of the dust plume, or to excessive aerosol emissions within the domain, or to an
 614 excessive inflow of desert aerosols at the domain boundaries. These hypotheses are
 615 investigated below. Another potential explanation may also be the uncertainties in the
 616 radiative properties of the dust aerosol incorporated in the CHIMERE model, or an
 617 underestimation of the aerosol deposition flux; these aspects are not investigated here.
 618
 619

3.4. Aerosol size distribution



620
 621 **Figure 8** - Aerosol volume size distribution for the AERONET station located in a)

622 Tamanrasset, b) Zinder, c) Banizoumbou and d) DakarBelair. t_A and t_m indicate the times of
623 the AERONET inversion product and the WRF-CHIMERE model respectively used for the
624 comparison. *wrf_chimere-G*, *wrf_chimere-M* and *wrf_chimere-C* refer to the WRF-CHIMERE
625 simulations using GOCART, MERRA2 and CAMS as dust aerosol initial and boundary
626 condition dataset respectively.

627

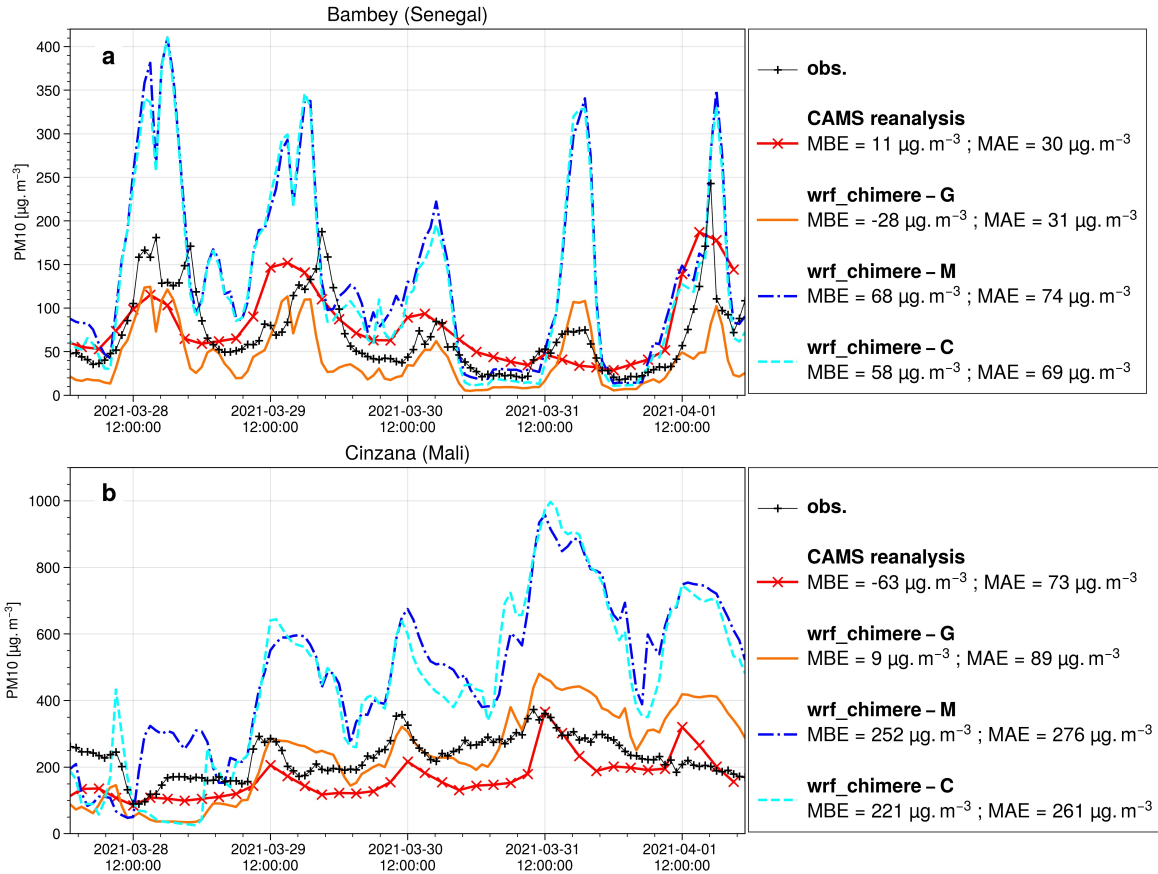
628 The evaluation of the aerosol size distribution in Fig. 8 shows that the simulations generally
629 have a dominant aerosol size mode shifted towards coarser sizes compared to the
630 AERONET inversion product. The ground-based size distribution has a strong peak between
631 1.14 μm and 5.00 μm , whereas the size distributions estimated by the WRF-CHIMERE
632 simulations peak for coarser aerosol. For the Dakar Belair station (Fig. 8d), the AERONET
633 inversion product indicates a first peak of lower intensity between 0.05 and 0.11 μm , which
634 suggests the presence of aerosols other than desert dust. These aerosols may be of
635 anthropogenic origin, given the proximity of the measurement site to the Senegalese capital.
636 When comparing the size distributions between the three simulations with different dust
637 aerosol initial and boundary condition dataset, it can be seen that the simulations driven with
638 CAMS and MERRA2 reanalysis are relatively close and well separated from the one driven
639 with the GOCART climatology. Notably, the dominant size bin in the simulation using
640 GOCART dataset is consistently the largest particles, whereas with the aerosol from
641 reanalyses, it is the aerosols between 5 μm and 10 μm . Consequently, the uncertainty
642 associated with the selection of the dust aerosol initial and boundary condition dataset is
643 high when examining the aerosol size distribution, particularly for particles exceeding 5.00
644 μm in diameter. The aforementioned uncertainties in the aerosol size distribution, which are
645 linked to the choice of the dust aerosol initial and boundary conditions dataset, may be
646 attributed to differences in the flow of desert dust entering the domain, as well as
647 uncertainties in the transfer method carried out by the CHIMERE model to match the aerosol
648 classes of these datasets to its own size distribution, described in section 2.2.3.

649 As a result, the shift in the WRF-CHIMERE size distribution towards coarser particles
650 compared to AERONET observations would result in a simulated AOD smaller than
651 AERONET measurements. However, the opposite is observed (section 3.3). This suggests a
652 positive bias in the simulated aerosol concentration, which would explain the positive bias in
653 the AOD, while the coarser size distribution would tend to compensate.

654

655

3.5. Aerosol concentrations

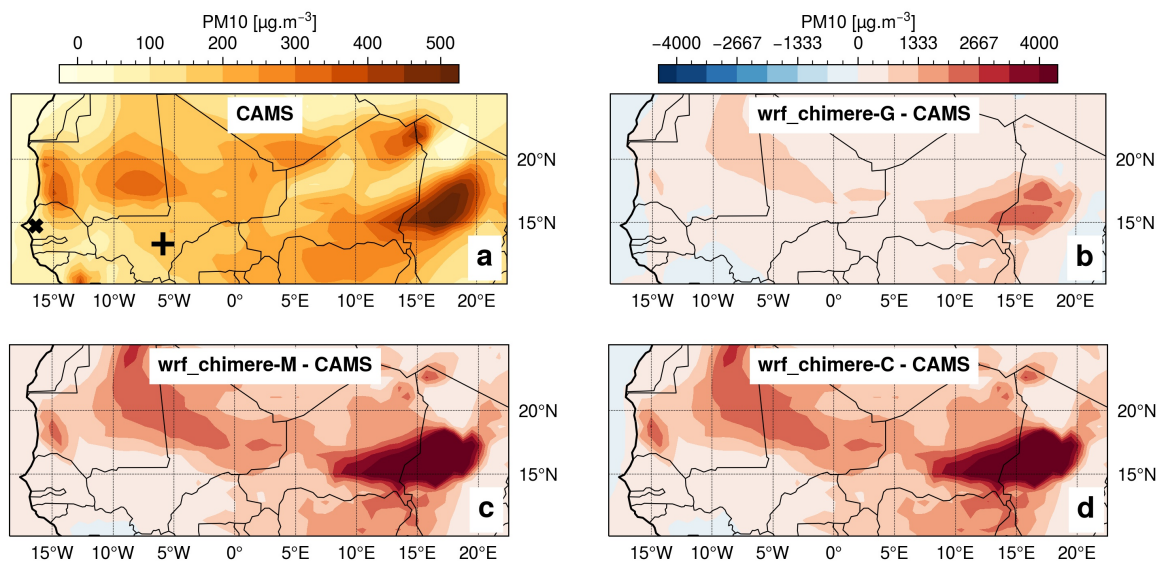


656
 657 **Figure 9** - Local comparison of CAMS reanalysis and simulated PM₁₀ surface concentrations
 658 with INDAAF network observations for a) Cinzana and b) Bambeey stations. *wrf_chimere-G*,
 659 *wrf_chimere-M* and *wrf_chimere-C* refer to the WRF-CHIMERE simulations using GOCART,
 660 MERRA2 and CAMS as dust aerosol initial and boundary condition dataset respectively.
 661 MBE is the mean bias error and MAE refers to the mean absolute error.

662
 663 The three simulations properly capture the dynamics of the PM₁₀ surface concentration with
 664 respect to the INDAAF ground measurement (Fig. 9) as correlation coefficients are around
 665 0.6 at Cinzana and close to 0.7 at Bambeey. The WRF-CHIMERE simulations driven with
 666 MERRA2 and CAMS dust aerosol datasets overestimate the surface PM₁₀ concentration
 667 peaks for Bambeey (Fig. 9a) and Cinzana (Fig. 9b), with high positive bias values of around
 668 63 g.m⁻³ at Bambeey and 247 g.m⁻³ at Cinzana. The latter station is closer to the dust
 669 aerosol sources. In contrast, the simulation using the GOCART dust aerosol dataset
 670 demonstrates superior performance in representing this variable, with an MAE that is
 671 approximately 60% and 70% lower than the two other simulations at Bambeey and Cinzana,
 672 respectively.

673 Furthermore, the uncertainty associated with the selection of initial and boundary condition
 674 dataset for dust aerosols is of a comparable magnitude to the simulation errors observed for
 675 surface PM₁₀ concentrations. Section 3.4 partly explains these discrepancies in surface PM₁₀
 676 concentration estimates between the simulation driven with the GOCART climatology and
 677 those driven with CAMS or MERRA2 reanalysis in terms of aerosol size distribution. These
 678 differences may also be attributed to variations in the size distribution of dust aerosol
 679 emissions or in the inflow of dust into the simulation domain and its aerosol size distribution.

680 Furthermore, Fig. 9 indicates that the CAMS reanalysis provides reliable estimates of
 681 surface PM₁₀ concentration, as evidenced by the fact it has the lowest MAE values.
 682 However, the Bambey and Cinzana ground measurements, which are the only two available
 683 for the case study, are situated at a considerable distance from the dust sources, limiting our
 684 ability to assess the accuracy of the CAMS reanalysis in capturing the dust event. Moreover,
 685 the CAMS reanalysis exhibits a negative bias at Cinzana, which is the closest site to the dust
 686 sources.
 687



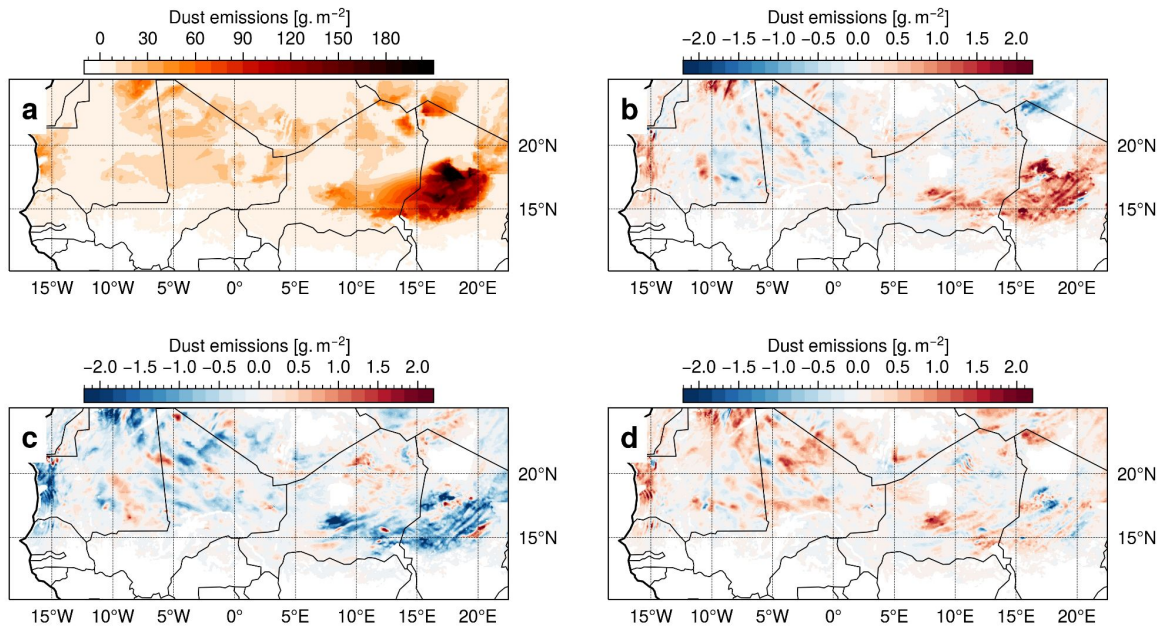
688 **Figure 10** - a) Mean from March 28th-00 UTC to April 2nd-00 UTC 2021 of CAMS reanalysis
 689 PM₁₀ surface concentration; x refers to the Bambey and + corresponds to Cinzana INDAAF
 690 stations. For panels b, c and d, PM₁₀ surface concentration mean differences from March
 691 28th-00 UTC to April 2nd-00 UTC 2021 between each of the WRF-CHIMERE simulations
 692 driven by GOCART, MERRA2 and CAMS, respectively, and the CAMS reanalysis.
 693

694
 695 Figure 10 illustrates an overestimation of the PM₁₀ concentrations as compared to the CAMS
 696 reanalysis. This is particularly evident in dust source areas such as the Bodele Depression.
 697 The WRF-CHIMERE simulation driven with the GOCART dataset is the closest to the CAMS
 698 reanalysis, with a mean estimate 3.6 times higher. However, this ratio reaches 8.6 for the
 699 simulations driven with the CAMS and MERRA2 reanalysis dataset.

700 The mean standard deviation between the three WRF-CHIMERE simulations is 35% of their
 701 mean PM₁₀ surface concentration estimate. Consequently the uncertainty in the estimation of
 702 dust PM₁₀ surface concentration associated with the selection of the dust aerosol initial and
 703 boundary condition dataset is significant. The discrepancies between the simulation using
 704 the GOCART climatology and the two other ones using CAMS or MERRA2 reanalysis can
 705 be partly explained by the differences in the simulated aerosol size distribution, as shown in
 706 section 3.4.

707
 708

3.6. Dust emissions

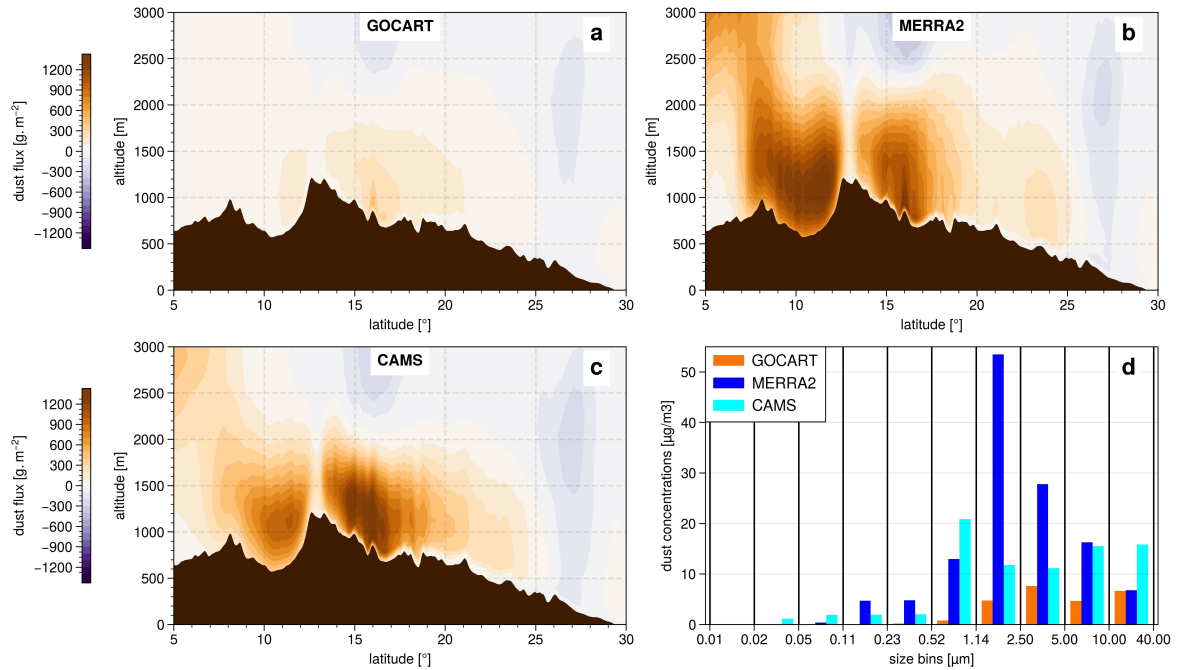


709
 710 **Figure 11** - a) Total dust emissions flux from March 28th-00 UTC to April 2nd-00 UTC 2021,
 711 averaged between the three WRF-CHIMERE simulations. For panels b, c and d, total dust
 712 emissions individual differences between each of the WRF-CHIMERE simulations driven by
 713 GOCART, MERRA2 and CAMS, respectively, and the mean of the three WRF-CHIMERE
 714 simulations.

715
 716 In terms of dust emissions (Fig. 11), the Bodele Depression is, as expected, identified as
 717 the primary dust source area, with emissions reaching up to 244 g/m². The differences of the
 718 simulations with each of the three dust aerosol initial and boundary conditions dataset,
 719 relative to their mean, exhibit highest values in the source zones located at the Bodele
 720 Depression and the South Atlas. Nevertheless, it is worth noting that there is a factor of 100
 721 in between the emissions in the Bodele area (approximately 200g/m²) and the observed
 722 differences between the three simulations. Consequently, the uncertainties in dust emissions
 723 resulting from the choice of the dust aerosol initial and boundary conditions dataset can be
 724 considered negligible. As emissions are primarily influenced by surface wind, it can be
 725 inferred that the uncertainty generated by the dust aerosol driving dataset on the surface
 726 wind is negligible too, which is confirmed by Fig. S4. Additionally, the size distributions of the
 727 aerosols emitted during the case study are found to be identical (not shown). Therefore, the
 728 differences in dust surface concentration and dust aerosol size distribution may be partly
 729 attributed to the dust flows at the boundaries of the domain and are not linked to differences
 730 in simulated dust emissions within the domain. However, there is no observational data
 731 available to enable a quantitative evaluation of the accuracy of the emissions computed
 732 within the WRF-CHIMERE simulations.

733
 734

3.7. Dust boundary flux



735
 736 **Figure 12** - Cumul of the dust flux at the eastern boundary of the simulation from March
 737 28th-00 UTC to April 2nd-00 UTC 2021 for the WRF-CHIMERE simulation with a) GOCART,
 738 b) MERRA2 and c) CAMS as dust aerosol initial and boundary conditions dataset; d) Dust
 739 size distribution at the eastern boundary limit average during the case study period, from the
 740 surface to 200hPa and over latitude. In panel abc, the dust flux is derived as the product
 741 between the dust aerosol concentration and the zonal wind, and positive values of the dust
 742 flow indicate a flow entering the simulation domain.

743
 744 As shown in Fig. 1b, the dust event is associated with a strong Harmattan flow,
 745 characterised by a northeasterly flow in the lower layer. It is thus interesting to quantify the
 746 dust inflow associated with each of the dust aerosol initial and boundary conditions dataset
 747 for the eastern domain boundary. The lowest dust flux is observed with GOCART (Fig. 12a),
 748 with a maximum of approximately 480 g/m^2 . In contrast, MERRA2 and CAMS (Fig. 14 b
 749 and c respectively) exhibit higher dust fluxes, with maximum values of around 1650 g/m^2 .
 750 The maximum flow is around 10°N for MERRA2, while for CAMS, it is closer to 16°N . Given
 751 that GOCART is a climatology, it is reasonable to expect a lower dust flux compared to the
 752 CAMS and MERRA2 reanalyses, which are real case simulations incorporating data
 753 assimilation of AOD. This is particularly true for the presented case study, which involves an
 754 intense dust event associated with a Harmattan flow.

755 There are also significant differences in both quantity and distribution by aerosol size bin
 756 (Fig. 12d). MERRA2 exhibits a strong dominant mode for the class between $1.14 \mu\text{m}$ and
 757 $2.50 \mu\text{m}$, while CAMS shows significant values from $0.52 \mu\text{m}$ to $40 \mu\text{m}$, with a maximum for
 758 the size class between $0.52 \mu\text{m}$ and $1.14 \mu\text{m}$. Finally, the GOCART model displays a lower
 759 variability between $1.14 \mu\text{m}$ and $40.00 \mu\text{m}$, with the maximum occurring for the size class
 760 between $2.55 \mu\text{m}$ and $5.00 \mu\text{m}$.

761 The eastern dust fluxes at the boundary significantly vary depending on the dataset used as
 762 dust aerosol initial and boundary conditions, both in terms of quantity and size distribution.
 763 The reanalysis dataset, CAMS and MERRA2, are expected to provide a more accurate
 764 representation of dust flux in terms of quantity as they are real case simulations assimilating

765 observational data in their calculations, as compared to GOCART which is a climatology.
766 However, GOCART provides a more comprehensive description of aerosol size distribution
767 with seven classes, in comparison to CAMS, which has only three classes but proposes a
768 higher horizontal resolution. While GOCART considers the effect of aerosol size to be
769 essential, CAMS assumes the horizontal resolution to be a key parameter. MERRA2 is the
770 most comprehensive of the three datasets, with the highest horizontal resolution, and an
771 aerosol size distribution that is close to the GOCART one with five classes.
772 As a result, and in consideration of the negligible uncertainty in dust emissions within the
773 simulation domain related to the choice of the dataset for dust aerosol initial and boundary
774 conditions (see 3.6), these differences in eastern dust fluxes appear to account for the
775 uncertainties of the simulated surface dust concentrations (see 3.5) and dust aerosol size
776 distribution (see 3.4).

777

778 **3.8. Discussions**

779 The evaluation of the simulated GHI at the Zagtouli solar power plant and the Banizoumbou
780 site (Fig. 2) indicates a significant enhancement in surface solar irradiance estimation when
781 WRF is coupled with CHIMERE. Specifically, the local MAE is reduced by approximately
782 75%. This confirms the relevance of incorporating the dust radiative effect with a coupling
783 approach, in comparison with the operational forecasts currently employed based on
784 meteorological models alone. During the dry season, dust events similar to the one
785 presented here, with emissions at Bodele and then transport of the plume westwards, are
786 common. This work therefore calls for forecasters in the photovoltaic sector to better account
787 for the desert dust cycle in their forecast products. This local evaluation also highlights the
788 potential benefits of using a regional model rather than a global product, as the WRF-
789 CHIMERE simulations outperform the CAMS gridded solar radiation product with an average
790 MAE reduced by approximately 38% at the Zagtouli solar farm and by 70% at the
791 Banizoumbou site, which is closer to dust sources. These discrepancies are corroborated by
792 the regional comparison presented in Figure 3, which reveals that the mean WRF-CHIMERE
793 GHI estimate is 5% lower than the CAMS solar radiation dataset. Additionally, the latter does
794 not exhibit a geographical pattern with lower GHI estimation along the dust plume trajectory,
795 in contrast to the WRF-CHIMERE simulations. These results confirm those from Sawadogo
796 et al. (2023) who recently showed that the CAMS reanalysis have low performances in
797 estimating solar irradiance during high AOD episodes like the one studied here.
798 Furthermore, the comparison reveals that incorporating dust in the simulation reduces
799 surface solar irradiance by 18% in this case study. This reduction is notably higher but
800 remains within the same order of magnitude as previous studies that integrated dust aerosol
801 information for solar estimation. For example, Masoom et al. (2021) in India and Mostamandi
802 et al. (2023) in the Arabian Peninsula reported GHI reductions due to dust of approximately
803 5-10%. This discrepancy underscores the potential variability of the dust impact on solar
804 irradiance depending on the method used to account for dust effects in the simulations. In
805 light of the anticipated expansion of PV production in West Africa, this point underscores the
806 potential consequences of such dust events if they are not accurately predicted.

807

808 The evaluation of local surface temperature (Fig. 4) reveals contrasting results regarding the
809 effectiveness of the coupled approach. It demonstrates an average local MAE reduction of
810 approximately 10% compared to the WRF-only simulation. However, the main differences
811 occur mainly at night, when no photovoltaic is produced, as previously observed by Yue et
812 al. (2010) and Briant et al. (2017). It can be attributed to the opposing radiative forcing

813 effects of dust aerosols across different wavelength ranges. In the case of longwave, which
814 corresponds to terrestrial radiation, the presence of dust aerosols has a warming effect.
815 Conversely, for shortwave, which corresponds to solar radiation, the presence of dust
816 aerosols induces a cooling effect. Consequently, during night-time when solely terrestrial
817 radiation is present, there is an increase in surface temperature. During day-time a
818 competition between the warming effect of terrestrial radiation and the cooling effect of solar
819 radiation ensues. The net impact is a decrease in surface temperature, indicating that the
820 effect of solar radiation dominates, with the cooling effect exceeding the warming effect
821 (Sokolik and Toon, 1999).

822 The regional evaluation in Fig. 5 confirms these contrasting results and indicates a reduction
823 of regional MAE by about 14% with the coupling rather than WRF alone. The overestimation
824 of surface temperature in dusty areas with the coupling, not present in the WRF only
825 simulation, reveals the dominant aerosol warming effect during night time as compared to
826 the cooling effect during daytime. These results align with those of Briant et al. (2017), who
827 estimated dust-induced warming of up to +5°C during nighttime and cooling of approximately
828 -1°C during daytime in a 2012 dust event in West Africa. These statements strongly depend
829 on the accuracy of the ERA5 reanalysis which serves as reference. ERA5 integrates data
830 assimilation of temperature and incorporates aerosol radiative effects through prescribed
831 monthly climatologies from the GOCART model, but does not dynamically simulate aerosols.
832 Due to the limited ground measurements in the Saharan region to constrain the reanalysis,
833 and to the significant biases that can come when considering a coarse climatology for the
834 radiative effects of aerosols to represent an intense dust event, it is possible that ERA5
835 underestimates the aerosol effect in dusty areas.

836
837 Nevertheless, despite the improvements demonstrated in solar irradiance and surface
838 temperature estimation, the WRF-CHIMERE simulations exhibit a notable positive bias in
839 terms of AOD, as evidenced by the local and regional evaluations presented in Figs. 6 and
840 7. This overestimation cannot be attributed solely to differences in aerosol concentrations, as
841 the simulations yield markedly disparate surface concentrations of PM₁₀, depending on the
842 dust aerosol initial and boundary condition dataset chosen (Fig. 10), while this discrepancies
843 do not appear in the AOD estimates. However, the results from Yahi et al. (2013) and Léon
844 et al. (2020) emphasized the importance of considering dust plume height when linking
845 surface PM₁₀ concentrations to AOD. Therefore, differences in the vertical distribution of the
846 dust plume, not evaluated in this study due to the lack of quantitative observational data,
847 could account for part of the observed discrepancies between simulated AODs and surface
848 PM₁₀ concentrations. This excess of aerosol load may be attributed to an overestimation of
849 emissions within the domain, but this cannot be verified as there is not any such
850 measurement. The incoming flux of dust in the domain plays a minor role as shown in Fig.
851 12 where the flux significantly also varies depending on the dust aerosol initial and boundary
852 condition dataset employed, while these differences are not any more present in the
853 simulated AOD estimates. Additionally, the underestimation of aerosol deposition, by
854 sedimentation (not studied in this research) could be at the origin of the overestimation of the
855 simulated dust loads. Finally, another potential explanation for these AOD biases may be the
856 inaccuracies in the dust radiative properties incorporated in the CHIMERE model calculation
857 (see Table S1 and S2). These depend on the mineralogical composition of the desert dust
858 particles emitted, which are considered uniform in this work. The radiative properties of
859 aerosols also depend on their granulometry. In the CHIMERE model, dust aerosols are
860 treated as spherical particles in the calculation of their radiative properties using Mie theory,

861 which introduces biases. Adbiyi et al. (2023) showed that ellipsoidal dust particles have a
862 slightly higher mass extinction efficiency compared to spherical particles. As a result,
863 accounting for ellipsoidal dust aerosols would lead to a slight increase in AOD associated
864 with a small decrease in GHI. This study further indicates that dust particles with radii
865 smaller than 20.0 μm are the primary contributors to dust AOD for shortwave radiation, with
866 the contribution from larger particles being an order of magnitude lower. Therefore, including
867 particles larger than 40.0 μm in the CHIMERE model would not significantly affect AOD and
868 GHI estimates. This is corroborated by Mostamandi et al. (2023), who demonstrated that
869 dust particles with radii smaller than 3 μm are primarily responsible for the reduction in solar
870 irradiance, while particles larger than 10 μm mainly contribute to dust deposition, which was
871 not examined in this study.

872

873 The uncertainty associated with the choice of the large scale dust aerosol initial and
874 boundary condition dataset is very low when considering the variables of interest for solar
875 production, namely GHI and surface temperature (Fig. 3 and 5). This uncertainty is also low
876 compared to the performance of simulations for AOD estimation (Fig. 7). This result is similar
877 when examining dust emissions within the domain, which are nearly identical for the three
878 coupled simulations (Fig. 11). This can be explained by the fact that dust emissions depend
879 on the cube of surface wind speed (Marticorena and Bergametti, 1995) which present no
880 significant signature of the selection of the dust aerosol initial and boundary conditions (Fig.
881 S4). The aerosols emitted within the chosen domain are much greater than those entering,
882 as the domain accounts for the main source zones. This is why the simulations are not that
883 sensitive to dust aerosol large-scale dataset employed. The results regarding the uncertainty
884 associated with the choice of the dust aerosol initial and boundary condition dataset differs
885 when examining various elements of the dust life cycle. Indeed, aerosol size distributions
886 vary significantly between the simulation driven with GOCART on one hand, and simulations
887 driven with CAMS and MERRA2 on the other hand. GOCART climatology over-represents
888 aerosols larger than 10 μm compared to the CAMS and MERRA2 reanalyses. These
889 differences partially account for the significant deviation in surface PM_{10} concentration
890 estimates (Fig. 10), indicating that reanalysis-type datasets result in much higher values, up
891 to 3 times higher, compared to climatological-type data which is closer to ground
892 observations. The dust flux entering the domain may also partly explain these differences. In
893 fact, this flux is very low with GOCART, with values up to 3.5 times lower than CAMS and
894 MERRA2 (Fig. 12). The size distribution of this incoming aerosol flux is also a determining
895 factor.

896

897 **4. Conclusion and perspectives**

898 This study aims to evaluate the ability of the WRF-CHIMERE coupling to simulate GHI
899 during a typical dust event in the dry season in West Africa. This event is characterised by a
900 Harmattan flux associated with significant desert dust emissions over the Bodele
901 Depression, with the dust plume subsequently transported westward. This work
902 demonstrates the utility of coupling a meteorological model with a desert aerosol life cycle
903 model to represent such events, particularly for improving solar forecasts. Indeed, GHI
904 estimations are markedly enhanced with this approach compared to using a meteorological
905 model alone with a 75% reduction of local MAE. Nevertheless, the performance of the WRF-
906 CHIMERE simulations in representing the aerosol load of this event is more controversial.
907 There is an overall overestimation of AOD and PM_{10} surface concentration by the coupled
908 model in the North Sahelian-Saharan zone.

909 This work also aims at investigating whether the performance of the simulations can be
910 improved by changing the dust aerosol initial and boundary condition dataset, and to
911 estimate the uncertainty associated with this choice. The results show that this selection has
912 almost no influence on the estimation of the solar irradiance, surface temperature and AOD.
913 On the contrary, the choice of the dust aerosol initial and boundary condition dataset has a
914 significant impact on the surface PM₁₀ concentration and the aerosol size distribution.

915

916 This work outlines new research perspectives. Firstly, we observe the difficulty of evaluating
917 simulations in West Africa due to the scarcity of available observations. Establishing a
918 denser measurement network or conducting observation campaigns, particularly for GHI,
919 would help research on solar estimation and forecasting in this region. Additionally, the
920 WRF-CHIMERE simulations demonstrate significant biases in terms of AOD and PM₁₀
921 surface concentration which are not fully explained here. One potential explanation for this is
922 an overestimation of dust emission, for which no evaluation is possible. Furthermore,
923 studying aerosol deposition (not conducted in this work) would complement the study of the
924 desert aerosol life cycle. On the one hand, an underestimation of deposition might be a
925 contributing factor to the overestimation of the simulated aerosol load. On the other hand,
926 dust deposition on solar panels affects solar production by masking the available solar
927 irradiance (soiling effect), and this should be taken into account in forecasting systems to
928 conduct optimised cleaning operations. A further limitation of this study is the use of the
929 WRF meteorological model for the coupling with CHIMERE, rather than the WRF-Solar
930 model (Jimenez et al., 2016), which is an enhanced version of WRF dedicated to solar
931 forecasting. Indeed, WRF-Solar incorporates enhanced algorithms for the computation of
932 solar irradiance, accounting for the direct and indirect effects of aerosols and employing an
933 advanced solar tracking algorithm. This makes it the appropriate version of WRF to use for
934 solar energy research. However, no coupling between WRF-Solar and CHIMERE has yet
935 been implemented, representing an important perspective to expend this work. Finally, the
936 study focuses on a typical dust event during the dry season, presenting essentially aerosol-
937 radiation interaction. It could be beneficial to test such simulation configuration for more
938 complex cases involving cloud presence. Indeed, the interaction between aerosols and
939 clouds have a significant impact on solar forecasting by increasing albedo, extending cloud
940 lifespan, and promoting cloud formation through increased condensation nucleus
941 concentration (indirect aerosol effects).

942

943 **Code and data availability**

944 WRF namelist configuration files, CHIMERE parameter files, Python codes exploited in this
945 study and GOCART climatology data can be found on the following Zenodo repository:
946 <https://zenodo.org/records/10808476>

947 ERA5 data can be found on the Copernicus Climate Data Store service :
948 <https://cds.climate.copernicus.eu/cdsapp#!/home>

949 CAMS data were downloaded on the Copernicus Atmosphere Data Store service :
950 <https://ads.atmosphere.copernicus.eu/cdsapp#!/home>

951 MERRA2 data can be found on the dedicated platform from NASA :
952 <https://goldsmr5.gesdisc.eosdis.nasa.gov/data/MERRA2/>

953 Data from AMMA ground measurements stations can be accessed from the dedicated
954 website : <https://amma-catch.osug.fr/-jeux-de-donnees->

955 INDAAF web page allows access to the data : <https://indaaf.obs-mip.fr/catalogue/>

956 AERONET data measurements and inversion products are available through the following
957 link: <https://aeronet.gsfc.nasa.gov/>

958 The MODIS satellite observations are available on the “Level-1 and Atmosphere Archive &
959 Distribution System Distributed Active Archive Center” platform from NASA :
960 <https://ladsweb.modaps.eosdis.nasa.gov/>

961

962 **Author contributions**

963 LC, SA, CL conceptualised the study. LC performed the simulations, the analysis and the
964 editions of the figures. LC, SA, CL, GB, BM, GS, CB, RL and JT discussed the results. LC
965 wrote the paper

966

967 **Competing interest**

968 The contact author has declared that none of the authors has any competing interests.

969

970 **Acknowledgment**

971 This work has been supported by the NETWAT project (ANR-22-CE03-0011) operated by
972 the French National Research Agency. To conduct the simulations, this study has benefited
973 from access to the IPSL-SU (SPIRIT) cluster within the IPSL Mesocentre ESPRI facility,
974 supported by the CNRS, UPMC, Labex L-IPSL, CNES and Ecole Polytechnique. The
975 authors want to thank the WRF and CHIMERE developers for giving free access to their
976 model. We thank the National Aeronautics and Space Agency for the availability of the
977 MODIS and the MERRA2 data, the European Center for Medium-Range Weather Forecasts
978 for the availability of the CAMS and ERA5 data and the investigators and staff who maintain
979 and provide the AERONET, the INDAAF and the AMMA-CATCH observational data. Finally,
980 we thank the Sonabel company for their contribution.

981 During the preparation of this work the authors used DeepL Write (DeepL SE) in order to
982 improve language and readability. After using this tool/service, the authors reviewed and
983 edited the content as needed and take full responsibility for the content of the publication.

984

985 **References**

986 Adebisi, A., Kok, J.F., Murray, B.J., Ryder, C.L., Stuut, J.-B.W., Kahn, R.A., Knippertz,
987 P., Formenti, P., Mahowald, N.M., Pérez García-Pando, C., Klose, M., Ansmann,
988 A., Samset, B.H., Ito, A., Balkanski, Y., Di Biagio, C., Romanias, M.N., Huang, Y.,
989 Meng, J., 2023. A review of coarse mineral dust in the Earth system. *Aeolian*
990 *Research* 60, 100849. <https://doi.org/10.1016/j.aeolia.2022.100849>

991 Africa Energy Outlook 2022, n.d.

992 Aidara, M.C., Fam, P.A., Danso, D.K., Mortey, E.M., Mbaye, A., Ndiaye, M.L.,
993 Bonkaney, A.L., Adamou, R., Anquetin, S., Diedhiou, A., 2023. Contribution to the
994 building of a weather information service for solar panel cleaning operations at
995 Diass plant (Senegal, Western Sahel). *Open Geosciences* 15.
996 <https://doi.org/10.1515/geo-2022-0449>

997 Alfaro, S.C., Gomes, L., 2001. Modeling mineral aerosol production by wind erosion:
998 Emission intensities and aerosol size distributions in source areas. *Journal of*
999 *Geophysical Research: Atmospheres* 106, 18075–18084.
1000 <https://doi.org/10.1029/2000JD900339>

1001 AMMA-CATCH (2005): Meteorological dataset (including radiative budget and soil
1002 variables), within the Niamey square degree site (16 000 km²), Niger. IRD, CNRS-
1003 INSU, OSUG, OMP, OREME. [doi:10.17178/AMMA-CATCH.AL.Met_Nc](https://doi.org/10.17178/AMMA-CATCH.AL.Met_Nc)

1004 Arakawa, A., 2004. The Cumulus Parameterization Problem: Past, Present, and Future.
1005 Journal of Climate 17, 2493–2525. [https://doi.org/10.1175/1520-0442\(2004\)017<2493:RATCPP>2.0.CO;2](https://doi.org/10.1175/1520-0442(2004)017<2493:RATCPP>2.0.CO;2)

1006

1007 Bergametti, G., Marticorena, B., Rajot, J.L., Chatenet, B., Féron, A., Gaimoz, C., Siour,
1008 G., Coulibaly, M., Koné, I., Maman, A., Zakou, A., 2017. Dust Uplift Potential in the
1009 Central Sahel: An Analysis Based on 10 years of Meteorological Measurements at
1010 High Temporal Resolution. Journal of Geophysical Research: Atmospheres 122,
1011 12,433-12,448. <https://doi.org/10.1002/2017JD027471>

1012 Bian, H., Prather, M.J., n.d. Fast-J2: Accurate Simulation of Stratospheric Photolysis in
1013 Global Chemical Models.

1014 Bou Karam, D., Flamant, C., Tulet, P., Chaboureau, J.-P., Dabas, A., Todd, M.C., 2009.
1015 Estimate of Sahelian dust emissions in the intertropical discontinuity region of the
1016 West African Monsoon. Journal of Geophysical Research: Atmospheres 114.
1017 <https://doi.org/10.1029/2008JD011444>

1018 Briant, R., Tuccella, P., Deroubaix, A., Khvorostyanov, D., Menut, L., Mailler, S.,
1019 Turquety, S., 2017. Aerosol–radiation interaction modelling using online coupling
1020 between the WRF 3.7.1 meteorological model and the CHIMERE 2016 chemistry-
1021 transport model, through the OASIS3-MCT coupler. Geoscientific Model
1022 Development 10, 927–944. <https://doi.org/10.5194/gmd-10-927-2017>

1023 Clauzel, L., Anquetin, S., Lavaysse, C., Tremoy, G., Raynaud, D., 2024. West African
1024 operational daily solar forecast errors and their link with meteorological conditions.
1025 Renewable Energy 224, 120101. <https://doi.org/10.1016/j.renene.2024.120101>

1026 d’Almeida, G.A., 1986. A Model for Saharan Dust Transport. Journal of Applied
1027 Meteorology and Climatology 25, 903–916. [https://doi.org/10.1175/1520-0450\(1986\)025<0903:AMFSDT>2.0.CO;2](https://doi.org/10.1175/1520-0450(1986)025<0903:AMFSDT>2.0.CO;2)

1028

1029 Dajuma, A., Yahaya, S., Touré, S., Diedhiou, A., Adamou, R., Konaré, A., Sido, M.,
1030 Golba, M., 2016. Sensitivity of Solar Photovoltaic Panel Efficiency to Weather and
1031 Dust over West Africa: Comparative Experimental Study between Niamey (Niger)
1032 and Abidjan (Côte d’Ivoire). Computational Water, Energy, and Environmental
1033 Engineering 5, 123–147. <https://doi.org/10.4236/cweee.2016.54012>

1034 Diabaté, L., Blanc, P., Wald, L., 2004. Solar radiation climate in Africa. Solar Energy 76,
1035 733–744.

1036 Diop, D., Drame, M.S., Diallo, M., Malec, D., Mary, D., Guillot, P., 2020. Modelling of
1037 Photovoltaic Modules Optical Losses Due to Saharan Dust Deposition in Dakar,
1038 Senegal, West Africa. Smart Grid and Renewable Energy 11, 89.
1039 <https://doi.org/10.4236/sgre.2020.117007>

1040 Dubovik, O., King, M.D., 2000. A flexible inversion algorithm for retrieval of aerosol
1041 optical properties from Sun and sky radiance measurements. Journal of

1042 Geophysical Research: Atmospheres 105, 20673–20696.
1043 <https://doi.org/10.1029/2000JD900282>

1044 Engelstaedter, S., Tegen, I., Washington, R., 2006. North African dust emissions and
1045 transport. Earth-Science Reviews 79, 73–100.
1046 <https://doi.org/10.1016/j.earscirev.2006.06.004>

1047 Engelstaedter, S., Washington, R., 2007. Atmospheric controls on the annual cycle of
1048 North African dust. Journal of Geophysical Research: Atmospheres 112.
1049 <https://doi.org/10.1029/2006JD007195>

1050 Evans, M., Knippertz, P., Akpo, A., Allan, R.P., Amekudzi, L., Brooks, B., Chiu, J.C.,
1051 Coe, H., Fink, A.H., Flamant, C., Jegede, O.O., Leal-Liousse, C., Lohou, F.,
1052 Kalthoff, N., Mari, C., Marsham, J.H., Yoboué, V., Zumsprekel, C.R., 2018. Policy
1053 findings from the DACCIWA Project. Zenodo.
1054 <https://doi.org/10.5281/ZENODO.1476843>

1055 El Alani, O., Ghennioui, A., Ghennioui, H., Saint-Drenan, Y.-M., Blanc, P., 2020.
1056 Evaluation of 24-hours forecasts of global solar irradiation from IFS, GFS and
1057 McClear models.

1058 Fécan, F., Marticorena, B., Bergametti, G., 1998. Parametrization of the increase of the
1059 aeolian erosion threshold wind friction velocity due to soil moisture for arid and
1060 semi-arid areas. Annales Geophysicae 17, 149–157.
1061 <https://doi.org/10.1007/s00585-999-0149-7>

1062 Flamant, C., Chaboureau, J.-P., Delanoë, J., Gaetani, M., Jamet, C., Lavaysse, C.,
1063 Bock, O., Borne, M., Cazenave, Q., Coutris, P., Cuesta, J., Menut, L., Aubry, C.,
1064 Benedetti, A., Bosser, P., Bounissou, S., Caudoux, C., Collomb, H., Donal, T.,
1065 Febvre, G., Fehr, T., Fink, A.H., Formenti, P., Araujo, N.G., Knippertz, P., Lecuyer,
1066 E., Andrade, M.N., Langué, C.G.N., Jonville, T., Schwarzenboeck, A., Takeishi, A.,
1067 2024. Cyclogenesis in the Tropical Atlantic: First Scientific Highlights from the
1068 Clouds–Atmospheric Dynamics–Dust Interactions in West Africa (CADDIWA) Field
1069 Campaign. Bulletin of the American Meteorological Society 105, E387–E417.
1070 <https://doi.org/10.1175/BAMS-D-23-0230.1>

1071 Gelaro, R., McCarty, W., Suárez, M.J., Todling, R., Molod, A., Takacs, L., Randles,
1072 C.A., Darmenov, A., Bosilovich, M.G., Reichle, R., Wargan, K., Coy, L., Cullather,
1073 R., Draper, C., Akella, S., Buchard, V., Conaty, A., Silva, A.M. da, Gu, W., Kim, G.-
1074 K., Koster, R., Lucchesi, R., Merkova, D., Nielsen, J.E., Partyka, G., Pawson, S.,
1075 Putman, W., Rienecker, M., Schubert, S.D., Sienkiewicz, M., Zhao, B., 2017. The
1076 Modern-Era Retrospective Analysis for Research and Applications, Version 2
1077 (MERRA-2). Journal of Climate 30, 5419–5454. <https://doi.org/10.1175/JCLI-D-16-0758.1>

1078

1079 Giles, D.M., Sinyuk, A., Sorokin, M.G., Schafer, J.S., Smirnov, A., Slutsker, I., Eck, T.F.,
1080 Holben, B.N., Lewis, J.R., Campbell, J.R., Welton, E.J., Korkin, S.V., Lyapustin,
1081 A.I., 2019. Advancements in the Aerosol Robotic Network (AERONET) Version 3
1082 database – automated near-real-time quality control algorithm with improved cloud

1083 screening for Sun photometer aerosol optical depth (AOD) measurements.
1084 Atmospheric Measurement Techniques 12, 169–209. [https://doi.org/10.5194/amt-](https://doi.org/10.5194/amt-12-169-2019)
1085 [12-169-2019](https://doi.org/10.5194/amt-12-169-2019)

1086 Ginoux, P., Chin, M., Tegen, I., Prospero, J.M., Holben, B., Dubovik, O., Lin, S.-J.,
1087 2001. Sources and distributions of dust aerosols simulated with the GOCART
1088 model. Journal of Geophysical Research: Atmospheres 106, 20255–20273.
1089 <https://doi.org/10.1029/2000JD000053>

1090 Hauglustaine, D.A., Hourdin, F., Jourdain, L., Filiberti, M.-A., Walters, S., Lamarque, J.-
1091 F., Holland, E.A., 2004. Interactive chemistry in the Laboratoire de Météorologie
1092 Dynamique general circulation model: Description and background tropospheric
1093 chemistry evaluation. Journal of Geophysical Research: Atmospheres 109.
1094 <https://doi.org/10.1029/2003JD003957>

1095 Hersbach, H., Bell, B., Berrisford, P., Hirahara, S., Horányi, A., Muñoz-Sabater, J.,
1096 Nicolas, J., Peubey, C., Radu, R., Schepers, D., Simmons, A., Soci, C., Abdalla, S.,
1097 Abellan, X., Balsamo, G., Bechtold, P., Biavati, G., Bidlot, J., Bonavita, M., De
1098 Chiara, G., Dahlgren, P., Dee, D., Diamantakis, M., Dragani, R., Flemming, J.,
1099 Forbes, R., Fuentes, M., Geer, A., Haimberger, L., Healy, S., Hogan, R.J., Hólm,
1100 E., Janisková, M., Keeley, S., Laloyaux, P., Lopez, P., Lupu, C., Radnoti, G., de
1101 Rosnay, P., Rozum, I., Vamborg, F., Villaume, S., Thépaut, J.-N., 2020. The ERA5
1102 global reanalysis. Quarterly Journal of the Royal Meteorological Society 146, 1999–
1103 2049. <https://doi.org/10.1002/qj.3803>

1104 Holben, B.N., Eck, T.F., Slutsker, I., Tanré, D., Buis, J.P., Setzer, A., Vermote, E.,
1105 Reagan, J.A., Kaufman, Y.J., Nakajima, T., Lavenu, F., Jankowiak, I., Smirnov, A.,
1106 1998. AERONET—A Federated Instrument Network and Data Archive for Aerosol
1107 Characterization. Remote Sensing of Environment 66, 1–16.
1108 [https://doi.org/10.1016/S0034-4257\(98\)00031-5](https://doi.org/10.1016/S0034-4257(98)00031-5)

1109 Hu, X.-M., Klein, P.M., Xue, M., 2013. Evaluation of the updated YSU planetary
1110 boundary layer scheme within WRF for wind resource and air quality assessments.
1111 Journal of Geophysical Research: Atmospheres 118, 10,490-10,505.
1112 <https://doi.org/10.1002/jgrd.50823>

1113 Iacono, M.J., Delamere, J.S., Mlawer, E.J., Shephard, M.W., Clough, S.A., Collins,
1114 W.D., 2008. Radiative forcing by long-lived greenhouse gases: Calculations with
1115 the AER radiative transfer models. Journal of Geophysical Research: Atmospheres
1116 113. <https://doi.org/10.1029/2008JD009944>

1117 Inness, A., Ades, M., Agustí-Panareda, A., Barré, J., Benedictow, A., Blechschmidt, A.-
1118 M., Dominguez, J.J., Engelen, R., Eskes, H., Flemming, J., Huijnen, V., Jones, L.,
1119 Kipling, Z., Massart, S., Parrington, M., Peuch, V.-H., Razinger, M., Remy, S.,
1120 Schulz, M., Suttie, M., 2019. The CAMS reanalysis of atmospheric composition.
1121 Atmos. Chem. Phys. 19, 3515–3556. <https://doi.org/10.5194/acp-19-3515-2019>

1122 Jiménez, P.A., Dudhia, J., González-Rouco, J.F., Navarro, J., Montávez, J.P., García-
1123 Bustamante, E., 2012. A Revised Scheme for the WRF Surface Layer Formulation.

1124 Monthly Weather Review 140, 898–918. <https://doi.org/10.1175/MWR-D-11->
1125 [00056.1](https://doi.org/10.1175/MWR-D-11-00056.1)

1126 Jimenez, P.A., Hacker, J.P., Dudhia, J., Haupt, S.E., Ruiz-Arias, J.A., Gueymard, C.A.,
1127 Thompson, G., Eidhammer, T., Deng, A., 2016. WRF-Solar: Description and Clear-
1128 Sky Assessment of an Augmented NWP Model for Solar Power Prediction. Bulletin
1129 of the American Meteorological Society 97, 1249–1264.
1130 <https://doi.org/10.1175/BAMS-D-14-00279.1>

1131 Kaly, F., Marticorena, B., Chatenet, B., Rajot, J.L., Janicot, S., Niang, A., Yahi, H.,
1132 Thiria, S., Maman, A., Zakou, A., Coulibaly, B.S., Coulibaly, M., Koné, I., Traoré, S.,
1133 Diallo, A., Ndiaye, T., 2015. Variability of mineral dust concentrations over West
1134 Africa monitored by the Sahelian Dust Transect. Atmos. Res. 164–165, 226–241.
1135 <https://doi.org/10.1016/j.atmosres.2015.05.011>

1136 Kandler, K., Benker, N., Bundke, U., Cuevas, E., Ebert, M., Knippertz, P., Rodríguez, S.,
1137 Schütz, L., Weinbruch, S., 2007. Chemical composition and complex refractive
1138 index of Saharan Mineral Dust at Izaña, Tenerife (Spain) derived by electron
1139 microscopy. Atmospheric Environment 41, 8058–8074.
1140 <https://doi.org/10.1016/j.atmosenv.2007.06.047>

1141 Klose, M., Shao, Y., Karremann, M.K., Fink, A.H., 2010. Sahel dust zone and synoptic
1142 background. Geophysical Research Letters 37.
1143 <https://doi.org/10.1029/2010GL042816>

1144 Klüser, L., Killius, N., Gesell, G., 2015. APOLLO_NG – a probabilistic
1145 interpretation of the APOLLO legacy for AVHRR heritage channels. Atmospheric
1146 Measurement Techniques 8, 4155–4170. <https://doi.org/10.5194/amt-8-4155-2015>

1147 Kok, J.F., Adebisi, A.A., Albani, S., Balkanski, Y., Checa-Garcia, R., Chin, M., Colarco,
1148 P.R., Hamilton, D.S., Huang, Y., Ito, A., Klose, M., Li, L., Mahowald, N.M., Miller,
1149 R.L., Obiso, V., Pérez García-Pando, C., Rocha-Lima, A., Wan, J.S., 2021.
1150 Contribution of the world’s main dust source regions to the global cycle of desert
1151 dust. Atmos. Chem. Phys. 21, 8169–8193. [https://doi.org/10.5194/acp-21-8169-](https://doi.org/10.5194/acp-21-8169-2021)
1152 [2021](https://doi.org/10.5194/acp-21-8169-2021)

1153 Lefèvre M., 2022, CAMS solar radiation evaluation and quality assurance report #34,
1154 March-May 2021, ECMWF COPERNICUS REPORT,
1155 [https://atmosphere.copernicus.eu/sites/default/files/custom-uploads/EQC-solar/](https://atmosphere.copernicus.eu/sites/default/files/custom-uploads/EQC-solar/CAMS2_73_2021SC1_D1.3.1-2021Q4_RAD_validation_report_MAM2021_v1.pdf)
1156 [CAMS2_73_2021SC1_D1.3.1-2021Q4_RAD_validation_report_MAM2021_v1.pdf](https://atmosphere.copernicus.eu/sites/default/files/custom-uploads/EQC-solar/CAMS2_73_2021SC1_D1.3.1-2021Q4_RAD_validation_report_MAM2021_v1.pdf)

1157 Legates, D.R., McCabe, G.J., 2013. A refined index of model performance: a rejoinder.
1158 International Journal of Climatology 33, 1053–1056.
1159 <https://doi.org/10.1002/joc.3487>

1160 Léon, J.-F., Martiny, N., Merlet, S., 2020. A Multi Linear Regression Model to Derive
1161 Dust PM10 in the Sahel Using AERONET Aerosol Optical Depth and CALIOP
1162 Aerosol Layer Products. Remote Sensing 12, 3099.
1163 <https://doi.org/10.3390/rs12183099>

1164 Marsham, J.H., Parker, D.J., Grams, C.M., Grey, W.M.F., Johnson, B.T., 2008.
1165 Observations of mesoscale and boundary-layer circulations affecting dust uplift and
1166 transport in the Saharan boundary layer (preprint). [https://doi.org/10.5194/acpd-8-
1167 8817-2008](https://doi.org/10.5194/acpd-8-8817-2008)

1168 Marticorena, B., Bergametti, G., 1995. Modeling the atmospheric dust cycle: 1. Design
1169 of a soil-derived dust emission scheme. *Journal of Geophysical Research:
1170 Atmospheres* 100, 16415–16430. <https://doi.org/10.1029/95JD00690>

1171 Marticorena, B., Chatenet, B., Rajot, J.L., Traoré, S., Coulibaly, M., Diallo, A., Koné, I.,
1172 Maman, A., NDiaye, T., Zakou, A., 2010. Temporal variability of mineral dust
1173 concentrations over West Africa: analyses of a pluriannual monitoring from the
1174 AMMA Sahelian Dust Transect. *Atmos. Chem. Phys.* 10, 8899–8915.
1175 <https://doi.org/10.5194/acp-10-8899-2010>

1176 Marticorena, B., Dorego, G.S., Rajot, J.L., Bouet, C., Allègre, M., Chatenet, B., Féron,
1177 A., Gaimoz, C., Siour, G., Valorso, R., Diop, M., Der Ba, S., Rokhy N'Diaye, G.,
1178 Séné, M. & Thiam, A. (2021). Air temperature, Bambey, Senegal. [dataset]. Aeris.
1179 <https://doi.org/10.25326/263>

1180 Marticorena, B., Dorego, G.S., Rajot, J.L., Bouet, C., Allègre, M., Chatenet, B., Féron,
1181 A., Gaimoz, C., Maisonneuve, F., Siour, G., Valorso, R., Diop, M., Der Ba, S.,
1182 Rokhy N'Diaye, G., Séné, M. & Thiam, A. (2021). PM10 concentration, Bambey,
1183 Senegal. [dataset]. Aeris. <https://doi.org/10.25326/267>

1184 Masoom, A., 2021. Forecasting dust impact on solar energy using remote sensing and
1185 modeling techniques. *Solar Energy* 16.

1186 Mazzeo, A., Burrow, M., Quinn, A., Marais, E.A., Singh, A., Ng'ang'a, D., Gatari, M.J.,
1187 Pope, F.D., 2022. Evaluation of the WRF and CHIMERE models for the simulation
1188 of PM_{2.5} in large East African urban conurbations. *Atmospheric Chemistry and
1189 Physics* 22, 10677–10701. <https://doi.org/10.5194/acp-22-10677-2022>

1190 Menut, L., 2023. Variability and combination as an ensemble of mineral dust forecasts
1191 during the 2021 CADDIWA experiment using the WRF 3.7.1 and CHIMERE
1192 v2020r3 models. *Geoscientific Model Development* 16, 4265–4281.
1193 <https://doi.org/10.5194/gmd-16-4265-2023>

1194 Menut, L., Bessagnet, B., Briant, R., Cholakian, A., Couvidat, F., Mailler, S., Pennel, R.,
1195 Siour, G., Tuccella, P., Turquety, S., Valari, M., 2021. The CHIMERE v2020r1
1196 online chemistry-transport model. *Geoscientific Model Development* 14, 6781–
1197 6811. <https://doi.org/10.5194/gmd-14-6781-2021>

1198 Menut, L., Siour, G., Mailler, S., Couvidat, F., Bessagnet, B., 2016. Observations and
1199 regional modeling of aerosol optical properties, speciation and size distribution over
1200 Northern Africa and western Europe. *Atmos. Chem. Phys.* 16, 12961–12982.
1201 <https://doi.org/10.5194/acp-16-12961-2016>

1202 MODIS Atmosphere Science Team, 2017. MODIS/Terra Aerosol Cloud Water Vapor
1203 Ozone Daily L3 Global 1Deg CMG. https://doi.org/10.5067/MODIS/MOD08_D3.061

1204 Mostamandi, S., Ukhov, A., Engelbrecht, J., Shevchenko, I., Osipov, S., Stenchikov, G.,
1205 2023. Fine and Coarse Dust Effects on Radiative Forcing, Mass Deposition, and
1206 Solar Devices Over the Middle East. *Journal of Geophysical Research:*
1207 *Atmospheres* 128, e2023JD039479. <https://doi.org/10.1029/2023JD039479>

1208 Mueller, R., Pfeifroth, U., Traeger-Chatterjee, C., 2015. Towards Optimal Aerosol
1209 Information for the Retrieval of Solar Surface Radiation Using Heliosat. *Atmosphere*
1210 6, 863–878. <https://doi.org/10.3390/atmos6070863>

1211 Niu, G.-Y., Yang, Z.-L., Mitchell, K.E., Chen, F., Ek, M.B., Barlage, M., Kumar, A.,
1212 Manning, K., Niyogi, D., Rosero, E., Tewari, M., Xia, Y., 2011. The community
1213 Noah land surface model with multiparameterization options (Noah-MP): 1. Model
1214 description and evaluation with local-scale measurements. *Journal of Geophysical*
1215 *Research: Atmospheres* 116. <https://doi.org/10.1029/2010JD015139>

1216 Ochiegbu, D.C., 2021. Event of harmattan dust transport in Kano State of Nigeria.
1217 *IJSRP* 11, 205–210. <https://doi.org/10.29322/IJSRP.11.08.2021.p11628>

1218 Plain, N., Hingray, B., Mathy, S., 2019. Accounting for low solar resource days to size
1219 100% solar microgrids power systems in Africa. *Renewable Energy* 131, 448–458.
1220 <https://doi.org/10.1016/j.renene.2018.07.036>

1221 Prigent, C., Jiménez, C., Catherinot, J., 2012. Comparison of satellite microwave
1222 backscattering (ASCAT) and visible/near-infrared reflectances (PARASOL) for the
1223 estimation of aeolian aerodynamic roughness length in arid and semi-arid regions.
1224 *Atmospheric Measurement Techniques* 5, 2703–2712. <https://doi.org/10.5194/amt-5-2703-2012>

1225

1226 Prospero, J.M., Ginoux, P., Torres, O., Nicholson, S.E., Gill, T.E., 2002. Environmental
1227 Characterization of Global Sources of Atmospheric Soil Dust Identified with the
1228 Nimbus 7 Total Ozone Mapping Spectrometer (toms) Absorbing Aerosol Product.
1229 *Reviews of Geophysics* 40, 2-1-2–31. <https://doi.org/10.1029/2000RG000095>

1230 Qu, Z., Oumbe, A., Blanc, P., Espinar, B., Gesell, G., Gschwind, B., Klüser, L., Lefèvre,
1231 M., Saboret, L., Schroedter-Homscheidt, M., Wald, L., 2017. Fast radiative transfer
1232 parameterisation for assessing the surface solar irradiance: The Heliosat-4 method.
1233 *Meteorologische Zeitschrift* 33–57. <https://doi.org/10.1127/metz/2016/0781>

1234 Rajot, J.L., Abdourhamane Touré, A., Marticorena, B., Bouet, C., Allègre, M., Chatenet,
1235 B., Féron, A., Gaimoz, C., Siour, G., Valorso, R., Maman, A. & Zakou, A. (2010). Air
1236 temperature, Banizoumbou, Niger. [dataset]. AERIS. <https://doi.org/10.25326/210>

1237 Rajot, J.L., Boubacar, A., Marticorena, B., Bouet, C., Allègre, M., Chatenet, B., Féron,
1238 A., Gaimoz, C., Siour, G., Valorso, R., Coulibaly, S.B., Kouyaté, Z., Coulibaly, B.,
1239 Coulibaly, M., Koné, I. & Traoré, S. (2010). Air temperature, Cinzana, Mali.
1240 [dataset]. AERIS. <https://doi.org/10.25326/269>

1241 Rajot, J.L., Boubacar, A., Marticorena, B., Bouet, C., Allègre, M., Chatenet, B., Féron,
1242 A., Gaimoz, C., Maisonneuve, F., Siour, G., Valorso, R., Coulibaly, S.B., Kouyaté,
1243 Z., Coulibaly, B., Coulibaly, M., Koné, I. & Traoré, S. (2010). PM10 concentration,
1244 Cinzana, Mali. [dataset]. AERIS. <https://doi.org/10.25326/268>

1245 Redelsperger, J.-L., Diedhiou, A., Flamant, C., Janicot, S., Lafore, J.-P., Lebel, T.,
1246 Polcher, J., Bourlès, B., Caniaux, G., Rosnay, P. de, Desbois, M., Eymard, L.,
1247 Fontaine, B., Geneau, I., Ginoux, K., Hoepffner, M., Kane, C.S.E., Law, K.S., Mari,
1248 C., Marticorena, B., Mougin, É., Pelon, J., Peugeot, C., Protat, A., Roux, F., Sultan,
1249 B., Akker, E. van den, 2006. Amma, une étude multidisciplinaire de la mousson
1250 ouest-africaine. *La Météorologie* 54, 22. <https://doi.org/10.4267/2042/20098>

1251 Sawadogo, W., Bliefernicht, J., Fersch, B., Salack, S., Guug, S., Diallo, B., Ogunjobi,
1252 Kehinde.O., Nakoulma, G., Tanu, M., Meilinger, S., Kunstmann, H., 2023. Hourly
1253 global horizontal irradiance over West Africa: A case study of one-year satellite-
1254 and reanalysis-derived estimates vs. in situ measurements. *Renewable Energy*
1255 216, 119066. <https://doi.org/10.1016/j.renene.2023.119066>

1256 Sawadogo, W., Fersch, B., Bliefernicht, J., Meilinger, S., Rummmler, T., Salack, S., Guug,
1257 S., Kunstmann, H., 2024. Evaluation of the WRF-solar model for 72-hour ahead
1258 forecasts of global horizontal irradiance in West Africa: A case study for Ghana.
1259 *Solar Energy* 271, 112413. <https://doi.org/10.1016/j.solener.2024.112413>

1260 Schepanski, K., Tegen, I., Todd, M.C., Heinold, B., Bönisch, G., Laurent, B., Macke, A.,
1261 2009. Meteorological processes forcing Saharan dust emission inferred from MSG-
1262 SEVIRI observations of subdaily dust source activation and numerical models.
1263 *Journal of Geophysical Research: Atmospheres* 114.
1264 <https://doi.org/10.1029/2008JD010325>

1265 Schroedter-Homscheidt, M., Azam, F., Betcke, J., Harrieder, N., Lefevre, M., Saboret,
1266 L., Saint-Drenan, Y.-M., 2022. Surface solar irradiation retrieval from MSG/SEVIRI
1267 based on APOLLO Next Generation and HELIOSAT-4 methods. *Meteorologische*
1268 *Zeitschrift* 31, 455–476.

1269 Shao, Y., Lu, H., 2000. A simple expression for wind erosion threshold friction velocity.
1270 *Journal of Geophysical Research: Atmospheres* 105, 22437–22443.
1271 <https://doi.org/10.1029/2000JD900304>

1272 Skamarock, W.C., Klemp, J.B., Dudhia, J., Gill, D.O., Barker, D.M., Duda, M.G., Huang,
1273 X.-Y., Wang, W., Powers, J.G., n.d. A Description of the Advanced Research WRF
1274 Version 3.

1275 Sokolik, I.N., Toon, O.B., 1999. Incorporation of mineralogical composition into models
1276 of the radiative properties of mineral aerosol from UV to IR wavelengths. *J.*
1277 *Geophys. Res.* 104, 9423–9444. <https://doi.org/10.1029/1998JD200048>

1278 The Paris Agreement | UNFCCC [WWW Document], n.d. URL
1279 <https://unfccc.int/process-and-meetings/the-paris-agreement> (accessed 2.12.24).

1280 Thompson, G., Eidhammer, T., 2014. A Study of Aerosol Impacts on Clouds and
1281 Precipitation Development in a Large Winter Cyclone. *Journal of the Atmospheric*
1282 *Sciences* 71, 3636–3658. <https://doi.org/10.1175/JAS-D-13-0305.1>

1283 Tuccella, P., Menut, L., Briant, R., Deroubaix, A., Khvorostyanov, D., Mailler, S., Siour,
1284 G., Turquety, S., 2019. Implementation of Aerosol-Cloud Interaction within WRF-
1285 CHIMERE Online Coupled Model: Evaluation and Investigation of the Indirect

1286 Radiative Effect from Anthropogenic Emission Reduction on the Benelux Union.
1287 Atmosphere 10, 20. <https://doi.org/10.3390/atmos10010020>

1288 Vautard, R., Bessagnet, B., Chin, M., Menut, L., 2005. On the contribution of natural
1289 Aeolian sources to particulate matter concentrations in Europe: Testing hypotheses
1290 with a modelling approach. Atmospheric Environment 39, 3291–3303.
1291 <https://doi.org/10.1016/j.atmosenv.2005.01.051>

1292 Washington, R., Todd, M.C., 2005. Atmospheric controls on mineral dust emission from
1293 the Bodélé Depression, Chad: The role of the low level jet. Geophysical Research
1294 Letters 32. <https://doi.org/10.1029/2005GL023597>

1295 Washington, R., Todd, M.C., Lizcano, G., Tegen, I., Flamant, C., Koren, I., Ginoux, P.,
1296 Engelstaedter, S., Bristow, C.S., Zender, C.S., Goudie, A.S., Warren, A., Prospero,
1297 J.M., 2006. Links between topography, wind, deflation, lakes and dust: The case of
1298 the Bodélé Depression, Chad. Geophysical Research Letters 33.
1299 <https://doi.org/10.1029/2006GL025827>

1300 Wild, O., Zhu, X., Prather, M.J., n.d. Fast-J: Accurate Simulation of In- and Below-Cloud
1301 Photolysis in Tropospheric Chemical Models.

1302 Willis, P.T., Tattelman, P., 1989. Drop-Size Distributions Associated with Intense
1303 Rainfall. Journal of Applied Meteorology (1988-2005) 28, 3–15.

1304 Yahi, H., Marticorena, B., Thiria, S., Chatenet, B., Schmechtig, C., Rajot, J.L., Crepon,
1305 M., 2013. Statistical relationship between surface PM10 concentration and aerosol
1306 optical depth over the Sahel as a function of weather type, using neural network
1307 methodology. Journal of Geophysical Research: Atmospheres 118, 13,265-13,281.
1308 <https://doi.org/10.1002/2013JD019465>

1309 Yang, D., Bright, J.M., 2020. Worldwide validation of 8 satellite-derived and reanalysis
1310 solar radiation products: A preliminary evaluation and overall metrics for hourly data
1311 over 27 years. Solar Energy, Special Issue on Grid Integration 210, 3–19.
1312 <https://doi.org/10.1016/j.solener.2020.04.016>

1313 Yue, X., Wang, H., Liao, H., Fan, K., 2010. Simulation of dust aerosol radiative feedback
1314 using the GMOD: 2. Dust-climate interactions. Journal of Geophysical Research:
1315 Atmospheres 115. <https://doi.org/10.1029/2009JD012063>

1316 Yushchenko, A., De Bono, A., Chatenoux, B., Kumar Patel, M., Ray, N., 2018. GIS-
1317 based assessment of photovoltaic (PV) and concentrated solar power (CSP)
1318 generation potential in West Africa. Renewable and Sustainable Energy Reviews
1319 81, 2088–2103. <https://doi.org/10.1016/j.rser.2017.06.021>

1320 Zhang, L., Gong, S., Padro, J., Barrie, L., 2001. A size-segregated particle dry
1321 deposition scheme for an atmospheric aerosol module. Atmospheric Environment
1322 35, 549–560. [https://doi.org/10.1016/S1352-2310\(00\)00326-5](https://doi.org/10.1016/S1352-2310(00)00326-5)

1323 Ziane, A., Necaibia, A., Sahouane, N., Dabou, R., Mostefaoui, M., Bouraiou, A., Khelifi,
1324 S., Rouabhia, A., Blal, M., 2021. Photovoltaic output power performance
1325 assessment and forecasting: Impact of meteorological variables. Solar Energy 220,
1326 745–757. <https://doi.org/10.1016/j.solener.2021.04.004>